Probing macroscopic quantum states with a sub-Heisenberg accuracy

Haixing Miao,[1] Stefan Danilishin,[2,3] Helge Müller-Ebhardt,[3] Henning Rehbein,[3] Kentaro Somiya,[4] and Yanbei Chen[4]

[1]*School of Physics, University of Western Australia, Western Australia 6009, Australia*

[2]*Physics Faculty, Moscow State University, Moscow RU-119991, Russia*

[3]*Max-Planck Institut für Gravitationsphysik (Albert-Einstein-Institut) and Leibniz Universität Hannover,*
Callinstrasse 38, D-30167 Hannover, Germany

[4]*Theoretical Astrophysics 130-33, California Institute of Technology, Pasadena, California 91125, USA*

Significant achievements in high-sensitivity measurements will soon allow us to probe quantum behaviors of macroscopic mechanical oscillators. In a recent work [Phys. Rev. A **80**, 043802 (2009)], we formulated a general framework for treating preparation of Gaussian quantum states of macroscopic oscillators through linear position measurements. To outline a complete procedure for testing macroscopic quantum mechanics, here we consider a subsequent verification stage which probes the prepared macroscopic quantum state and verifies the quantum dynamics. By adopting an optimal time-dependent homodyne detection in which the phase of the local oscillator varies in time, the conditional quantum state can be characterized below the Heisenberg limit, thereby achieving a quantum tomography. In the limiting case of no readout loss, such a scheme evades measurement-induced back action, which is identical to the variational-type measurement scheme invented by Vyatchanin *et al.* [JETP **77**, 218 (1993)] but in the context for detecting gravitational waves. To motivate macroscopic quantum mechanics experiments with future gravitational-wave detectors, we mostly focus on the parameter regime where the characteristic measurement frequency is much higher than the oscillator frequency and the classical noises are Markovian, which captures the main feature of a broadband gravitational-wave detector. In addition, we discuss verifications of Einstein-Podolsky-Rosen-type entanglement between macroscopic test masses in future gravitational-wave detectors, which enables us to test one particular version of gravity decoherence conjectured by Diósi [Phys. Lett. **A120**, 377 (1987)] and Penrose [Gen. Rel. Grav. **28**, 581 (1996)].

PACS number(s): 03.65.Ta, 42.50.Dv, 03.65.Ud, 04.80.Nn

I. INTRODUCTION

Due to recent significant advancements in fabricating low-loss optical, electrical, and mechanical devices, we will soon be able to probe behaviors of macroscopic mechanical oscillators in the quantum regime. This will not only shed light on quantum-limited measurements of various physical quantities, such as a weak force, but also help us to achieve a better understanding of quantum mechanics on macroscopic scales.

As a premise of investigating macroscopic quantum mechanics (MQM), the mechanical oscillator should be prepared close to being in a pure quantum state. To achieve this, there are mainly three approaches raised in the literature: (i) The first and the most transparent approach is to cool down the oscillator by coupling it to an additional heat bath that has a temperature T_{add} much lower than that of the environment T_0. As a result, the oscillator will achieve an effective temperature given by $T_{eff} = (T_0 \gamma_m + T_{add} \Gamma_{add})/(\gamma_m + \Gamma_{add})$ with γ_m and Γ_{add} denoting the damping due to coupling to the environment and the additional heat bath, respectively. In the strong-damping regime with $\Gamma_{add} \gg \gamma_m$, we achieve the desired outcome with $T_{eff} \approx T_{add}$. Since the typical optical frequency ω_0 can be much higher than $k_B T_0/\hbar$, a coherent optical field can be effectively served as a zero-temperature heat bath. Indeed, by coupling an oscillator parametrically to an optical cavity, many state-of-the-art experiments have demonstrated significant cooling of the oscillator, achieving a very low thermal occupation number [1–16]. A similar mechanism also applies to electromechanical systems, as demonstrated in several experiments [17–19].

(ii) The second approach is to introduce additional damping via feedback (i.e., so-called cold-damping). The feedback loop modifies the dynamics of the oscillator in a way similar to the previous cooling case. Such an approach has also been realized experimentally [20–22]. If the intrinsic mechanical and electrical/optical qualities of the coupled system are high, those cooling and cold-damping experiments can eventually achieve the quantum ground state of a mechanical oscillator [23–28]. (iii) The third approach is to construct a conditional quantum state of the mechanical oscillator via continuous position measurements. Quantum mechanically, if the oscillator position is being continuously monitored, a certain classical trajectory in phase space can be mapped out, and the oscillator is projected into a *posteriori* state, [29] which is also called a conditional quantum state [30–35]. Given an ideal continuous measurement without loss, the resulting conditional quantum state of the oscillator is a pure state.

Recently, we theoretically investigated the third approach for general linear position measurements in great detail [35]. The analysis of this work is independent of the scale and mass of the oscillator—these parameters will only modify the structure of arising noises. In particular, we applied our formalism to discuss MQM experiments with macroscopic test masses in future gravitational-wave (GW) detectors. We demonstrated explicitly that given the noise budget for the design sensitivity, next-generation GW detectors such as the Advanced LIGO [36] and Cryogenic Laser Interferometer Observatory (CLIO) [37] can prepare nearly pure Gaussian
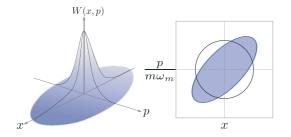
FIG. 1. (Color online) A schematic plot of a Wigner function $W(x, p)$ (left) and the corresponding uncertainty ellipse (right) for the covariance matrix $\mathbf{V}^{\text{cond}}$ (which can be viewed as a projection of the Wigner function). The center of the plot is given by the conditional mean $(x^{\text{cond}}, p^{\text{cond}})$. The Heisenberg limit is shown in a unit circle with radius given by the zero-point fluctuation $\sqrt{\hbar/(2m\omega_m)}$. For a pure Gaussian conditional quantum state, the area of the ellipse [i.e., $\pi \det \mathbf{V}^{\text{cond}}/(2m\omega_m)^2$] is also equal to that of the Heisenberg limit. Therefore, the uncertainty product $\det \mathbf{V}^{\text{cond}}$ can serve as an appropriate figure of merit for quantifying purity of a quantum state.

quantum states and create Einstein-Podolsky-Rosen-type entanglement between macroscopic test masses. In addition, we showed that the free-mass *standard quantum limit* (SQL) [38–40] for the detection sensitivity,

$$S_x^{\text{SQL}}(\Omega) = \frac{2\hbar}{m\Omega^2},\qquad(1)$$

where m is mass of the probing test mass and Ω is the detection frequency, also serves as a benchmark for MQM experiments with GW detectors.

More concretely, a Gaussian conditional quantum state is fully described by its Wigner function as shown schematically in Fig. 1. It is given by

$$W(x, p) = \frac{1}{2\pi\sqrt{\det \mathbf{V}^{\text{cond}}}} \exp\left[-\frac{1}{2}\vec{X}\mathbf{V}^{\text{cond}-1}\vec{X}^T\right].\qquad(2)$$

Here $\vec{X} = [x - x^{\text{cond}}, p - p^{\text{cond}}]$ with x^{cond} and p^{cond} denoting conditional means of oscillator position x and momentum p, and $\mathbf{V}^{\text{cond}}$ is the covariance matrix between position and momentum. Purity of the conditional quantum state can be quantified by the uncertainty product, which is defined as

$$U \equiv \frac{2}{\hbar}\sqrt{\det \mathbf{V}^{\text{cond}}} = \frac{2}{\hbar}\sqrt{V_{xx}^{\text{cond}} V_{pp}^{\text{cond}} - V_{xp}^{\text{cond}2}},\qquad(3)$$

which is also proportional to square root of the area of the uncertainty ellipse as shown in Fig. 1. In Ref. [35], this uncertainty product is related to the SQL-beating ratio of the classical noises of the measurement device. In addition, the amount of entanglement between test objects is related to the size of the frequency window (ratio between upper and lower ends of that frequency window) in which the classical noise goes below the SQL.

A state-preparation stage alone does not provide a complete test of MQM. This is because the measurement data in the state-preparation process only allow us to measure a classical trajectory of the oscillator—quantum fluctuations are only inferred from the noise budget; they are not directly visible. Therefore, the resulting conditional quantum state critically relies on the noise model of the measurement device. If such

a noise model is imprecise, it will yield severe discrepancies between the actual quantum state and the conditional one. Therefore, it calls for a second measurement stage, which has to follow the preparation stage. In this paper, we will address this issue by considering a subsequent state-verification procedure, in which we establish the tomography of the conditional quantum state obtained during the preparation stage. On the one hand, this verification stage can serve as a check of the specific noise model to verify the prepared quantum state. On the other hand, if we insert an evolution stage with the oscillator evolving freely before the verification, the quantum dynamics of the oscillator can also be probed, which allows us to study different decoherence effects and also check whether a macroscopic mechanical oscillator does evolve in the same way as a quantum harmonic oscillator or not.

Since the conditional quantum state undergoes a random walk in phase space as shown schematically in Fig. 2, classical information of the conditional mean, obtained by the preparer from the measurement data, needs to be passed onto the verifier who will then proceed with the tomography. Suppose the state preparation stage ends at $t = 0$ and the preparer obtains a conditional quantum whose Wigner function is $W[x(0), p(0)]$. The task of the verifier is to try to reconstruct this Wigner function by synthesizing marginal distributions of different mechanical quadratures $\hat{X}_\zeta(0)$ from ensemble measurements at $t > 0$, and

$$\hat{X}_\zeta(0) \equiv \hat{x}(0)\cos\zeta + \frac{\hat{p}(0)}{m\omega_m}\sin\zeta,\qquad(4)$$

where $\hat{x}(0)$ and $\hat{p}(0)$ denote oscillator position and momentum, respectively, at $t = 0$ and ω_m is the oscillation frequency. This process is similar to the optical quantum tomography where different optical quadratures are measured with homodyne detections [41]. However, there is one significant difference— mechanical quadratures are not directly accessible with linear position measurements, which measure

$$\hat{x}_q(t) = \hat{x}(0)\cos\omega_m t + \frac{\hat{p}(0)}{m\omega_m}\sin\omega_m t\qquad(5)$$
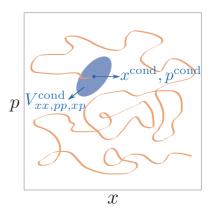

FIG. 2. (Color online) A schematic plot of the random walk of the conditional quantum state (i.e., its Wigner function) in phase space. Its center is given by the conditional mean $[x^{\text{cond}}(t), p^{\text{cond}}(t)]$, with its uncertainty given by conditional variances $V_{xx,pp,xp}^{\text{cond}}$. To verify the prepared conditional quantum state, the only knowledge that the verifier needs to know is classical information of the conditional mean provided by the preparer if the noises are Markovian.

rather than $\hat{X}_\zeta$. To probe mechanical quadratures, we propose the use of a time-dependent homodyne detection with the local-oscillator phase varying in time. Given a measurement duration of T_{int}, we can construct an integral estimator, which reads

$$\hat{X} = \int_0^{T_{\text{int}}} dt \, g(t) \hat{x}(t) \propto \hat{x}(0) \cos \zeta' + \frac{\hat{p}(0)}{m\omega_m} \sin \zeta' \qquad (6)$$

with $\cos \zeta' \equiv \int_0^{T_{\text{int}}} dt \, g(t) \cos \omega_m t$ and $\sin \zeta' \equiv \int_0^{T_{\text{int}}} dt \, g(t) \sin \omega_m t$. Therefore, a mechanical quadrature $\hat{X}_{\zeta'}$ is probed [cf. Eq. (4)]. Here $g(t)$ is some filtering function, and it is determined by the time-dependent homodyne phase and also the way in which data at different time are combined.

The ability to measure mechanical quadratures does not guarantee success of a verification process. In order to recover the prepared quantum state, it requires a verification accuracy below the Heisenberg limit. Physically, the output of the verification process is a sum of the mechanical-quadrature signal and some uncorrelated Gaussian noise. Mathematically, it is equivalent to applying a Gaussian filter onto the original Wigner function $W(x, p)$ of the prepared state [42], and thus the reconstructed Wigner function is

$$W_{\text{recon}}(x, p) = \int_{-\infty}^{\infty} dx' dp' \psi(x - x', p - p') W(x', p'), \qquad (7)$$

where the Gaussian filter $\psi(x, p)$ is given by

$$\psi(x, p) \equiv \frac{1}{2\pi \sqrt{\det \mathbf{V}^{\text{add}}}} \exp\left[-\frac{1}{2} \vec{\xi} \mathbf{V}^{\text{add}-1} \vec{\xi}^T \right] \qquad (8)$$

with $\vec{\xi} = [x, p]$ and $\mathbf{V}^{\text{add}}$ denoting the covariance matrix for the added verification noise. If the prepared quantum state is Gaussian, by using the property of Gaussian integration, the reconstructed Wigner function reads

$$W_{\text{recon}}(x, p) = \frac{1}{2\pi \sqrt{\det \mathbf{V}^{\text{recon}}}} \exp\left[-\frac{1}{2} \vec{\xi} \mathbf{V}^{\text{recon}-1} \vec{\xi}^T \right], \qquad (9)$$

and the covariance matrix $\mathbf{V}^{\text{recon}}$ is

$$\mathbf{V}^{\text{recon}} = \mathbf{V}^{\text{cond}} + \mathbf{V}^{\text{add}}. \qquad (10)$$

In Fig. 3, we show schematically the effects of different levels of verification accuracy given the same prepared conditional
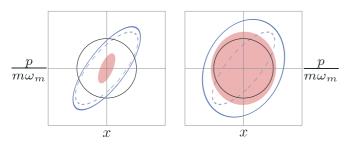

FIG. 3. (Color online) A schematic plot of the uncertainty ellipses of reconstructed states with the same prepared Gaussian quantum state but different levels of verification accuracy, which shows the necessity of a sub-Heisenberg accuracy. The center of the plot is given by the conditional mean ($x^{\text{cond}}, p^{\text{cond}}$). The shaded regimes correspond to the verification accuracy. The Heisenberg limit is shown by a unit circle. The dashed and solid ellipses represent the prepared state and the reconstructed states, respectively.
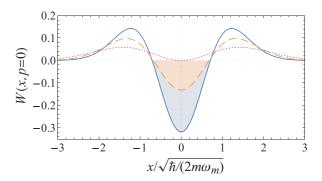

FIG. 4. (Color online) Values of reconstructed Wigner functions on the $p = 0$ plane [i.e., $W_{\text{recon}}(x, p = 0)$] for a single-quantum state, obtained at different levels of verification accuracy. The solid curve shows the ideal case with no verification error. Dashed and dotted curves correspond to cases with verification errors of $1/4$ and $1/2$ of the Heisenberg limit, respectively. The negative regime (shaded) or the nonclassicality vanishes as the verification error increases. This again manifests the importance of a sub-Heisenberg verification accuracy.

quantum state. A sub-Heisenberg accuracy, with an error area smaller than the Heisenberg limit, is essential for us to obtain a less distorted understanding of the original prepared quantum state. In addition, if the prepared quantum state of the mechanical oscillator is non-Gaussian [43–47], sub-Heisenberg accuracy is a necessary condition for unveiling the nonclassicality of the quantum state, as shown schematically in Fig. 4 and proved rigorously in Appendix A.

Verifications of quantum states below the Heisenberg limit also naturally allow us to test whether entanglement between two macroscopic test masses in GW detectors can indeed be established, as predicted in Ref. [34,35], and how long such an entangled state can survive. Survival of macroscopic entanglement can test one particular version of gravity decoherence conjectured by Diósi [48] and Penrose [49]. For an individual object, it is not entirely clear into what classical superposition of *pointer* states gravity decoherence will drive it. For an entangled state among multiple objects, even though Gaussian, it would naturally have to decay into the one that is not entangled, within the gravity decoherence time scale.

As we will show, in order to achieve sub-Heisenberg accuracy, we need to optimize the local-oscillator phase of the time-dependent homodyne detection as well as the weight with which data collected at different time will be combined. If there is no readout loss, this optimization automatically will give a detection scheme that evades measurement-induced back action, the same as the variational-type measurement scheme proposed by Vyatchanin and Matsko [50] for detecting gravitational-wave signals with known arrival time. Since in a single measurement setup different quadratures do not commute with each other, namely

$$[\hat{X}_\zeta, \hat{X}_{\zeta'}] = \frac{i\hbar}{m\omega_m} \sin(\zeta - \zeta'), \qquad (11)$$

one needs multiple setups and each makes ensemble measurements of one particular quadrature $\hat{X}_\zeta$ with a sub-Heisenberg

accuracy; the synthesis of these measurements yields a quantum tomography.

As a sequence to Ref. [35] and to motivate MQM experiments with future GW detectors, we will also focus on the same parameter regime where the characteristic measurement frequency is much higher than the oscillator frequency and the oscillator can be treated as a free mass. In addition, we will consider situations where the spectra of the classical noise can be modeled as being white. Non-Markovianity of noise sources—although they certainly arise in actual GW detectors [35] and will be crucial for the success of a real experiment—is a rather technical issue. The non-Markovianity will not change the results presented here significantly, as we will show and address in a separate paper [51].

This paper is organized as follows: In Sec. II, we will formulate the system model mathematically by writing down the Heisenberg equations of motion; in Sec. III, we will provide a timeline for a full MQM experiment with preparation, evolution, and verification stages and use simple order-of-magnitude estimates to show that this experimental proposal is indeed plausible; in Sec. V, we will evaluate the verification accuracy in the presence of Markovian noises (largely confirming the order-of-magnitude estimates, but with precise numerical factors); in Sec. VI, we will consider verifications of macroscopic quantum entanglement between test masses in GW detectors as a test of gravity decoherece; in Sec. VII, we will summarize our main results. In the Appendix, we will present mathematical details for solving integral equations that we encounter in obtaining the optimal verification scheme.

II. MODEL AND EQUATIONS OF MOTION

In this section, we will present a mathematical description of the system model, as shown schematically in the upper left panel of Fig. 5. The oscillator position is linearly coupled to coherent optical fields through radiation pressure. Meanwhile, information of the oscillator position flows into the outgoing optical fields continuously. This models a measurement process in an optomechanical system without a cavity or with a large-bandwidth cavity. The corresponding Heisenberg equations, valid for both preparation and verification stages, are formally identical to classical equations of motion except for that all quantities are Heisenberg operators. The oscillator position $\hat{x}$ and momentum $\hat{p}$ satisfy the following equations:

$$\dot{\hat{x}}(t) = \hat{p}(t)/m, \tag{12}$$

$$\dot{\hat{p}}(t) = -2\gamma_m \hat{p}(t) - m\omega_m^2 \hat{x}(t) + \alpha \hat{a}_1(t) + \hat{\xi}_F(t). \tag{13}$$

Here $\alpha \hat{a}_1$ corresponds to the quantum-radiation-pressure noise or so-called back-action noise; $\alpha \equiv (\hbar m \Omega_q^2)^{1/2} = (8 I_0 \omega_0 \hbar/c^2)^{1/2}$ is the coupling constant between the oscillator and optical fields with I_0 denoting the optical power and Ω_q quantifying the characteristic frequency of measurement strength. We have included the fluctuation-dissipation mechanism of the mechanical oscillator by introducing the mechanical damping rate γ_m and classical-force noise $\hat{\xi}_F$ (i.e., the Brownian thermal noise). In the Markovian limit,
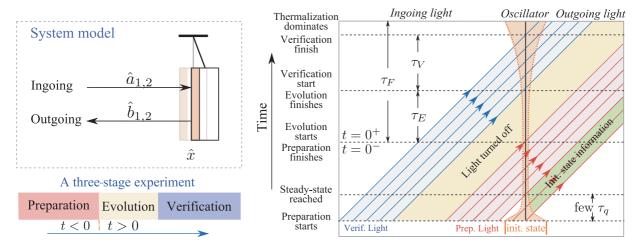

FIG. 5. (Color online) A schematic plot of the system (upper left panel) and the corresponding space-time diagram (right panel) showing the timeline of the proposed MQM experiment (see Sec. III A for detailed explanations). In this schematic plot, the oscillator position is denoted by $\hat{x}$, which is coupled to the optical fields through radiation pressure. The ingoing and outgoing optical fields are denoted by $\hat{a}_{1,2}$ and $\hat{b}_{1,2}$ with subscripts 1, 2 for the amplitude and phase quadratures, respectively. In the space-time diagram, the world line of the oscillator is shown by the middle vertical line. For clarity, ingoing and outgoing optical fields are represented by the left and right regions on the different sides of the oscillator world line, even though, in reality, optical fields escape from the same side as where they enter. We show light rays during preparation and verification stages in red and blue. In between, the yellow shaded region describes the evolution stage with the light turned off for a duration of τ_E. The conditional variance of the oscillator motion is represented by the shaded region alongside the central vertical line (not drawn to the same scale as the light propagation). At the beginning of the preparation, the conditional variance is dominated by that of the initial state (orange). After a transient, it is determined by incoming radiations and measurements. Right after state preparation, we show the expected growth of the conditional variance due to thermal noise alone, and ignoring the effect of back-action noise, which is evaded during the verification process. The verification stage lasts for a duration of τ_V, and it is shorter than τ_F, after which the oscillator will be dominated by thermalization.

the correlation function for $\hat{\xi}_F$ is given by[1]

$$\langle \hat{\xi}_F(t)\hat{\xi}_F(t')\rangle_{\text{sym}} = S_F^{\text{th}}\delta(t-t')/2, \quad (14)$$

where $S_F^{\text{th}} = 4m\gamma_m k_B T_0 \equiv 2\hbar m\Omega_F^2$ and we have defined a characteristic frequency Ω_F for the thermal noise.

The amplitude and phase quadratures of ingoing optical fields $\hat{a}_{1,2}$ and of outgoing optical fields $\hat{b}_{1,2}$ satisfy the following input-output relations:

$$\hat{b}_1(t) = \sqrt{\eta}\hat{n}_1(t) + \sqrt{1-\eta}\,\hat{a}_1(t), \quad (15)$$

$$\hat{b}_2(t) = \sqrt{\eta}\hat{n}_2(t) + \sqrt{1-\eta}\left[\hat{a}_2(t) + \frac{\alpha}{\hbar}\hat{x}(t) + \frac{\alpha}{\hbar}\hat{\xi}_x(t)\right]. \quad (16)$$

Here $\hat{n}_{1,2}$ originate from nonunity quantum efficiency of the photodetector for $\eta > 0$. In the paraxial and narrow-band approximation, $\hat{a}_{1,2}$ are related to the electrical-field strength at the central frequency ω_0 by [52–54]

$$\hat{E}(t) \equiv \left(\frac{4\pi\hbar\omega_0}{\mathcal{S}c}\right)^{1/2}\{[\bar{a} + \hat{a}_1(t)]\cos\omega_0 t + \hat{a}_2(t)\sin\omega_0 t\} \quad (17)$$

with $\bar{a}$ denoting the classical amplitude and $\mathcal{S}$ standing for the effective cross-section area of the laser beam. A similar relation also holds for the outgoing fields $\hat{b}_{1,2}$. In addition, they satisfy $[\hat{a}_1(t), \hat{a}_2(t')] = [\hat{b}_1(t), \hat{b}_2(t')] = i\delta(t-t')$. Their correlation functions read

$$\langle \hat{a}_i(t)\hat{a}_j(t')\rangle_{\text{sym}} = \delta_{ij}e^{\pm 2q}\delta(t-t')/2, \quad (i,j=1,2), \quad (18)$$

where q denotes the squeezing factor ($q = 0$ for a vacuum-state input) with "+" for the amplitude quadrature and "−" for the phase quadrature. Correspondingly, the correlation function for the back-action noise $\alpha\hat{a}_1$ is simply

$$\langle \alpha\hat{a}_1(t)\alpha\hat{a}_1(t')\rangle_{\text{sym}} = S_F^{\text{BA}}\delta(t-t')/2 \quad (19)$$

with $S_F^{\text{BA}} \equiv e^{2q}\hbar m\Omega_q^2$. In Eq. (16), $\hat{\xi}_x$ is the sensing noise. One example is the internal thermal noise, and it is defined as the difference between the center-of-mass motion and the surface motion of the oscillator which is actually being measured. In the Markovian approximation, it has the following correlation function:

$$\langle \hat{\xi}_x(t)\hat{\xi}_x(t')\rangle_{\text{sym}} = S_x^{\text{th}}\delta(t-t')/2, \quad (20)$$

where $S_x^{\text{th}} = \hbar/(m\Omega_x^2)$ and we introduce a characteristic frequency Ω_x for the sensing noise.

Note that the Ω_q, Ω_F, and Ω_x that we have introduced are also the frequencies at which the back-action noise, thermal noise, and sensing noise intersect the SQL [cf. Eq. (1)], respectively. They are identical to what were introduced in Ref. [35]. For conveniences of later discussions, we introduce the following dimensionless ratios:

$$\zeta_F = \Omega_F/\Omega_q, \quad \zeta_x = \Omega_q/\Omega_x. \quad (21)$$

In addition, we define two characteristic time scales for the measurement and thermal-noise strength as

$$\tau_q \equiv 1/\Omega_q, \quad \tau_F \equiv 1/\Omega_F. \quad (22)$$

---

[1] Here $\langle\ \rangle_{\text{sym}}$ stands for a *symmetrized* ensemble average. For a system characterized by a density matrix $\hat{\rho}$, it is defined as

$$\langle \hat{o}_1(t)\hat{o}_2(t')\rangle_{\text{sym}} \equiv \text{Tr}\left\{[\hat{o}_1(t)\hat{o}_2(t') + \hat{o}_2(t')\hat{o}_1(t)]\hat{\rho}\right\}/2.$$

III. OUTLINE OF THE EXPERIMENT WITH ORDER-OF-MAGNITUDE ESTIMATE

In this section, we will describe in details the timeline of a plausible MQM experiment (Sec. III A) and provide order-of-magnitude estimates of the conditional variance of the prepared quantum state, the evolution of the prepared quantum state, and the verification accuracy in the free-mass regime (Secs. III B, III C, and III D). This will provide qualitatively the requirements on the noise level for the success of an MQM experiment. We will give more rigorous treatments in the next section.

A. Timeline of proposed experiment

We have sketched a space-time diagram for the proposed MQM experiment in the right panel of Fig. 5—with time going upward; therefore we start from the bottom of the figure.

(i) **Lock Acquisition.** At the beginning, the mechanical oscillator is in a highly mixed state, so are the optical fields. Therefore, the first step is to "acquire lock" of the measurement device and reach a steady-state operation mode, during which several τ_q will have elapsed. From this time and on, initial-state information will have been forgotten (propagating outward within the green strip), and the state of the oscillator will be determined by the driving fields, including the classical-force noise and sensing noise, as well as the quantum noise. This will be the start of the state-preparation stage (region above the 45° green strip).

(ii) **State Preparation.** This stage is a steady-state operation of the measurement device. The quantum state of the oscillator is collapsed continuously due to homodyne readouts of the photocurrent. At any instant during state preparation, based on the measured history of the photocurrent (mostly on data within several times τ_q to the past of t), the conditional expectation (x^{cond}, p^{cond}) for the oscillator position $\hat{x}$ and momentum $\hat{p}$ can be constructed. The second moments, describable by the covariance matrix between position and momentum, which consists of V_{xx}^{cond}, V_{xp}^{cond}, and V_{pp}^{cond}, can be calculated from the noise model of the measurement device—they, together with x^{cond} and p^{cond}, fully determine the quantum state, that is, the Wigner function of the oscillator at any instant [cf. Eq. (2)]. For a Gaussian steady state, the construction of (x^{cond}, p^{cond}) and conditional covariance matrix from the history of the photocurrent can be accomplished most easily using Wiener filtering, as shown in Ref. [35].

The preparation stage terminates at $t = 0$, when (x^{cond}, p^{cond}) and the covariance matrix will be determined by data from several $-\tau_q$ up to 0 as shown by the red strip.

(iii) **State Evolution.** If we want to investigate the quantum dynamics of the oscillator and study various decoherence effects, we can delay the verification process and allow the oscillator to freely evolve with the interaction light turned off (represented by the yellow strip). During this period, the thermal noise will induce diffusions of the oscillator position and

momentum, thus increasing the conditional variance as shown schematically by broadening of the shaded region alongside the oscillator world line. If there were any additional decoherence effect, the variance would grow faster than the case with the thermal decoherence alone. A follow-up verification allows us to check whether additional decoherence mechanisms, such as the gravity decoherence conjectured by Diósi [48] and Penrose [49], exist or not.

(iv) **State Verification.** After the evolution stage, the verification stage starts (represented by blue strip). We intentionally use different colors to label the preparation light and verification light—symbolizing the fact that in principle, a different observer (verifier) could perform the verification process and verify the quantum state by himself or herself. The only knowledge from the preparer would be the conditional expectation x^{cond} and p^{cond} if all noise sources are Markovian. The verifier uses a time-dependent homodyne detection and collects the data from measuring the photocurrents. The verification process lasts for a time scale of τ_V between the characteristic measurement time scale τ_q and the thermal decoherence time scale τ_F, after which diffusions of $\hat{x}$ and $\hat{p}$ in the phase space become much larger than the Heisenberg limit. Based upon the measurement data, the verifier can construct an integral estimator for one particular mechanical quadrature [cf. Eq. (6)].

These three stages—preparation, evolution, and verification— have to be repeated for many times before enough data are collected to build up statistics. After finishing the experiment, the verifier will obtain a reconstructed quantum state of the mechanical oscillator, and then can proceed to compare with the preparer and interpret the results.

B. Order-of-magnitude estimate of the conditional variance

In this and the following two sections, we will provide order-of-magnitude estimates for a three-staged MQM experiment including preparation, evolution, and verification stages. This gives us physical insights into different time scales involved in an MQM experiment and also the qualitative requirements for an experimental realization. We will justify those estimates based upon more careful treatments in the next several sections.

Based upon the measurement data from several $-\tau_q$ to 0, one can construct a conditional quantum state for the mechanical oscillator. Suppose that the phase quadrature of the outgoing fields is being measured and the photodetection is ideal with $\eta = 0$. Given a measurement time scale of τ (measuring from $-\tau$ to 0), variances for the oscillator position and momentum at $t = 0$ in the free-mass regime with $\omega_m \to 0$ are approximately equal to [cf. Eqs. (12), (13), (15), and (16)]

$$\delta x^2(0) \sim S_x^{\text{tot}}/\tau + \tau^3 S_F^{\text{tot}}/m^2 \sim N_x^{\frac{3}{4}} N_F^{\frac{1}{4}} \delta x_q^2, \quad (23)$$

$$\delta p^2(0) \sim m^2 S_x^{\text{tot}}/\tau^3 + \tau S_F^{\text{tot}} \sim N_x^{\frac{1}{4}} N_F^{\frac{3}{4}} \delta p_q^2. \quad (24)$$

Here $S_F^{\text{tot}} \equiv S_F^{\text{BA}} + S_F^{\text{th}}$ [cf. Eqs. (14) and (19)] and $S_x^{\text{tot}} \equiv S_x^{\text{sh}} + S_x^{\text{th}}$ with S_x^{sh} denoting the shot noise due to $\hat{a}_2$

[cf. Eqs. (16) and (20)]; we have defined

$$N_x \equiv 1 + 2\zeta_x^2, \quad N_F \equiv 1 + 2\zeta_F^2, \quad (25)$$

while

$$\delta x_q^2 \equiv \hbar/(2m\Omega_q), \quad \delta p_q^2 \equiv \hbar m\Omega_q/2. \quad (26)$$

The optimal measurement time scale is given by $\tau \sim \tau_q$. Purity of the prepared conditional quantum state at $t = 0$ is approximately equal to [cf. Eq. (3)]

$$U(0) \sim \frac{2}{\hbar} \delta x(0) \delta p(0) \sim N_x N_F. \quad (27)$$

If classical noises are low, namely, $N_x \sim N_F \sim 1$, the conditional quantum state will be pure with $U(0) \sim 1$. For future GW detectors such as the Advanced LIGO, both ζ_x and ζ_F will be around 0.1, and such a low classical-noise budget clearly allows us to prepare nearly pure quantum states of the macroscopic test masses.

C. Order-of-magnitude estimate of state evolution

During the evolution stage, the uncertainty ellipse of the conditional quantum state will rotate at the mechanical frequency in phase space, and meanwhile there is a growth in the uncertainty due to thermal decoherence as shown schematically in Fig. 6. Given a strong measurement, the variance of the resulting conditional quantum state in position $\delta x^2(0)$ will be approximately equal to δx_q^2 as shown explicitly in Eq. (23) with $N_x, N_F \sim 1$. It is much smaller than the zero-point uncertainty of an ω_m oscillator, which is given by $\hbar/(2m\omega_m)$. Therefore, the conditional quantum state of the oscillator is highly squeezed in position. The position uncertainty contributed by the initial momentum will be comparable to that of the initial-position uncertainty after a evolution duration of τ_q. This can be directly seen from an order-of-magnitude estimate. In the free-mass regime,

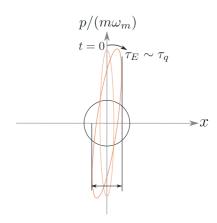$$\hat{x}(t) \sim \hat{x}(0) + \frac{\hat{p}(0)}{m} t. \quad (28)$$

FIG. 6. (Color online) Rotation and diffusion of a highly position-squeezed conditional quantum state prepared by a strong measurement with $\Omega_q \gg \omega_m$. The initial-momentum uncertainty will contribute an uncertainty in the position comparable to the initial position uncertainty when the evolution duration $\tau_E \sim \tau_q$.

For an evolution duration of τ_E, the corresponding variance in position is

$$\delta x^2(\tau_E) \sim \delta x^2(0) + \frac{\delta p^2(0)}{m^2}\tau_E^2 \sim \delta x^2(0)[1 + (\Omega_q\tau_E)^2].$$
(29)

The contribution from the initial-momentum uncertainty (the second term) will become important when $\Omega_q\tau_E \sim 1$ or equivalently $\tau_E \sim \tau_q$.

Apart from a rotation, the uncertainty ellipse will also grow due to thermal decoherence. Variances in the position and momentum contributed by thermal decoherence are approximately given by [cf. Eqs. (12) and (13)]

$$\delta x_{\rm th}^2(\tau_E) \sim \tau_E^3 S_F^{\rm th}/m^2 = \zeta_F^2(\Omega_q\tau_E)^3\delta x_q^2, \qquad (30)$$

$$\delta p_{\rm th}^2(\tau_E) \sim \tau_E S_F^{\rm th} = \zeta_F^2(\Omega_q\tau_E)\delta p_q^2. \qquad (31)$$

The growth in the uncertainty ellipse will simply be

$$U^{\rm th}(\tau_E) \sim \frac{2}{\hbar}\delta x_{\rm th}(\tau_E)\delta p_{\rm th}(\tau_E) \sim \zeta_F^2(\Omega_q\tau_E)^2 = (\tau_E/\tau_F)^2.$$
(32)

When $\tau_E > \tau_F$, $U^{\rm th}(\tau_E) > 1$ and the conditional quantum state will be dominated by thermalization.

If there were any additional decoherence effect, the growth in the uncertainty would be much larger than what has been estimated here. A subsequent verification stage can serve as a check.

D. Order-of-magnitude estimate of the verification accuracy

To verify the prepared conditional quantum state, the oscillator position needs to be measured for a finite duration to obtain information about $\hat{x}(0)$ and $\hat{p}(0)$ [cf. Eq. (5) and (6)] or about $\hat{x}(\tau_E)$ and $\hat{p}(\tau_E)$ if the evolution stage is inserted. In order for an entire state characterization to be possible, one might then expect that an oscillation period must pass, and during this period, the thermal noise should cause an insignificant diffusion of the oscillator momentum compared with its zero-point uncertainty, which requires [40]

$$\frac{k_B T_0}{\hbar\omega_m} < Q_m \qquad (33)$$

with $Q_m \equiv \omega_m/(2\gamma_m)$ denoting the mechanical quality factor. This requirement is unnecessary if the initial quantum state is prepared by a strong measurement. As we have mentioned in the previous section, the resulting condition quantum state is highly squeezed in position and the initial-momentum uncertainty will make a significant contribution to the uncertainty in position after $\tau > \tau_q$. This means, depending on the particular strategy, one can extract $\hat{x}$ and $\hat{p}$ below the levels of δx_q and δp_q, respectively, as long as one is able to measure oscillator position with an accuracy better than δx_q, within a time scale of several τ_q. This is certainly possible if the measurement-induced back action is evaded.

To evade the measurement-induced back action, one notices the fact that the amplitude quadrature $\hat{b}_1$ contains $\hat{a}_1$, which is responsible for the back action, and meanwhile the phase quadrature $\hat{b}_2$ contains the information of oscillator position, part of which is contributed by the back action [cf. Eqs. (12)–(16)]. Therefore, if we measure particular combinations of $\hat{b}_1$ and $\hat{b}_2$ at different times, by summing

up those measurements, we will be able to cancel the back action and obtain a back-action-evading (BAE) estimator for a given mechanical quadrature. Such a cancelation mechanism is only limited by the readout loss ($\eta \neq 0$), which introduces uncorrelated vacuum fluctuations.

We can make an order-of-magnitude estimate to show that a sub-Heisenberg accuracy can be indeed achieved. With the BAE technique, the force noise that limits the verification accuracy will only contain the thermal-noise part. Similar to Eqs. (23) and (24) but with $S_F^{\rm tot}$ replaced by $S_F^{\rm th}$, the variances in position and momentum during the verification stage are simply

$$\delta x_V^2 \sim S_x^{\rm tot}/\tau + \tau^3 S_F^{\rm th}/m^2 \sim N_x^{3/4}\zeta_F^{1/2}\delta x_q^2, \qquad (34)$$

$$\delta p_V^2 \sim m^2 S_x^{\rm tot}/\tau^3 + \tau S_F^{\rm th} \sim N_x^{1/4}\zeta_F^{3/2}\delta p_q^2. \qquad (35)$$

Here the optimal verification time scale would be $\tau_V \sim \zeta_F^{-1/2}\tau_q$ and $\tau_q < \tau_V < \tau_F$. A summarizing figure of merit for the verification accuracy is approximately given by

$$U^{\rm add}|_{\rm BAE} \sim \frac{2}{\hbar}\delta x_V\delta p_V \sim N_x^{1/2}\zeta_F. \qquad (36)$$

A sub-Heisenberg accuracy can be achieved when $\zeta_F < 1$. Note that this error can be arbitrarily small by lowering ζ_F indefinitely (i.e., a very strong measurement). If phase-squeezed light is injected during the verification stage, we would have

$$U^{\rm add}|_{\rm BAE} \sim \left(e^{-2q} + 2\zeta_x^2\right)^{1/2}\zeta_F = \sqrt{\frac{\Omega_F^2}{\Omega_q^2 e^{2q}} + \frac{2\Omega_F^2}{\Omega_x^2}}. \quad (37)$$

Increasing the squeezing factor always improves our verification sensitivity, with a limit of

$$U_{\rm lim}^{\rm add}|_{\rm BAE} \sim \Omega_F/\Omega_x = \zeta_x\zeta_F, \qquad (38)$$

which can be much lower than unity in the case of future GW detectors or any low-noise measurement device.

Had we not evaded the back-action noise, we would have $\sqrt{N_F}$ in the place of ζ_F, which means $\delta x_V\delta p_V$ would be Heisenberg-limited—unless different squeezing factors are assumed. For low squeezing (i.e., $e^{\pm 2q}$ larger than both ζ_x and ζ_F), we need phase squeezing for the $\hat{x}$ observation and amplitude squeezing for the $\hat{p}$ observation, with

$$U^{\rm add}|_{\rm without\,BAE} \sim e^{-q}, \qquad (39)$$

which is a significant factor ($1/\zeta_F$) worse than the BAE scheme. Even though there exists an optimal squeezing factor that this scheme can apply and yields

$$U_{\rm opt}^{\rm add}|_{\rm without\,BAE} \sim \zeta_x, \qquad (40)$$

it is still worse than the limiting situation of the BAE scheme [cf. Eq. (38)] by a factor of $1/\zeta_F(\gg 1)$.

IV. THE CONDITIONAL QUANTUM STATE AND ITS EVOLUTION

The previous order-of-magnitude estimates provide us a qualitative picture of an MQM experiment, especially in the free-mass regime where future GW detectors are operating. As long as ζ_F and ζ_x are smaller than unity, namely, the classical noise goes below the SQL around the most sensitive frequency

band ($\Omega \sim \Omega_q$) of the measurement device, not only can we prepare a nearly pure quantum state but we can also make a sub-Heisenberg tomography of the prepared state. In this and following sections, we will provide more rigorous treatments directly by analyzing the detailed dynamics of the system.

A. The conditional quantum state obtained from Wiener filtering

The rigorous mathematical treatment of state preparation has been given in Ref. [35]. The main idea is to treat the conditional quantum state preparation as a classical filtering problem, which is justified by the fact that the outgoing optical quadratures $\hat{b}_{1,2}$ at different times commute with each other, the same as a classical random process. For such a Gaussian linear system, the Wiener filter, satisfying the minimum mean-square error criterion, allows us to obtain an optimal estimate for the quantum state of the oscillator (i.e., the conditional quantum state). Based upon the measurement data $y(t)$ ($t < 0$), conditional means for oscillator position and momentum at $t = 0$ can be constructed as [cf. Eq. (14) of Ref. [35]]

$$x^{\text{cond}}(0) \equiv \langle \hat{x}(0) \rangle^{\text{cond}} = \int_{-\infty}^{0} dt\, K_x(-t) y(t), \quad (41)$$

$$p^{\text{cond}}(0) \equiv \langle \hat{p}(0) \rangle^{\text{cond}} = \int_{-\infty}^{0} dt\, K_p(-t) y(t). \quad (42)$$

Here K_x and K_p are causal Wiener filters. The covariance matrix is given by [cf. Eq. (15) of Ref. [35]]

$$\mathbf{V}^{\text{cond}}_{o_i o_j}(0) = \langle \hat{o}_i(0)\hat{o}_j(0) \rangle^{\text{cond}}_{\text{sym}} - \langle \hat{o}_i(0) \rangle^{\text{cond}} \langle \hat{o}_j(0) \rangle^{\text{cond}}, \quad (43)$$

where $i, j = 1, 2$ and $\hat{o}_1, \hat{o}_2$ denote $\hat{x}, \hat{p}$, respectively. In the free-mass regime, we showed that [cf. Eq. (52)–(54) in Ref. [35]]

$$\mathbf{V}^{\text{cond}}(0) = \begin{bmatrix} N_F^{\frac{1}{4}} N_x^{\frac{3}{4}} \sqrt{2}\delta x_q^2 & N_F^{\frac{1}{2}} N_x^{\frac{1}{2}} \hbar/2 \\ N_F^{\frac{1}{2}} N_x^{\frac{1}{2}} \hbar/2 & N_F^{\frac{3}{4}} N_x^{\frac{1}{4}} \sqrt{2}\delta p_q^2 \end{bmatrix}. \quad (44)$$

With conditional means and variances, the Wigner function, or equivalently the conditional quantum state, is uniquely defined [cf. Eq. (2)]. Correspondingly, purity of the conditional quantum state is quantified by

$$U(0) = \frac{2}{\hbar}\sqrt{\det \mathbf{V}^{\text{cond}}(0)} = N_x N_F. \quad (45)$$

This simply justifies the order-of-magnitude result presented in Eq. (27).

B. Evolution of the conditional quantum state

In the following discussions, we will analyze how such a conditional quantum state evolves during the evolution stage. On the one hand, this confirms the qualitative results presented in the Sec. III C. On the other hand, it provides a quantitative understanding of the time scale for the later verification stage.

The equations of motion for the oscillator during the evolution stage are given by Eqs. (12) and (13) except that

there is no radiation pressure, for the light is turned off.[2] For simplicity and also a consideration of the case in a realistic experiment, we will assume an oscillator with a high quality factor (i.e., $\omega_m \gg \gamma_m$). Within a time scale much shorter than $1/\gamma_m$, the oscillator can be well approximated as a free oscillator. Correspondingly, the analytical solution to oscillator position reads

$$\hat{x}(t) = \hat{x}_q(t) + \int_0^\infty dt'\, G_x(t - t') \hat{\xi}_F(t'). \quad (46)$$

Here the free quantum oscillation $\hat{x}_q(t)$ of the oscillator is given by Eq. (5). We have defined the Green's function as

$$G_x(t) = \Theta(t) \frac{\sin(\omega_m t)}{m\omega_m}, \quad (47)$$

with $\Theta(t)$ denoting the Heaviside function.

Given an evolution duration of τ_E, from Eq. (14) and Eq. (46) the corresponding covariance matrix evolves as

$$\mathbf{V}(\tau_E) = \mathbf{R}_\Phi^T \, \mathbf{V}^{\text{cond}}(0) \, \mathbf{R}_\Phi$$
$$+ \frac{S_F^{\text{th}}}{8m^2\omega_m^3} \begin{bmatrix} 2\Phi - \sin 2\Phi & 2m\omega_m \sin^2 \Phi \\ 2m\omega_m \sin^2 \Phi & m^2\omega_m^2 (2\Phi + \sin 2\Phi) \end{bmatrix}, \quad (48)$$

where $\Phi \equiv \omega_m \tau_E$ and the rotation matrix $\mathbf{R}_\Phi$ is given by

$$\mathbf{R}_\Phi = \begin{bmatrix} \cos\Phi & -m\omega_m \sin\Phi \\ (m\omega_m)^{-1}\sin\Phi & \cos\Phi \end{bmatrix}. \quad (49)$$

The first term in Eq. (48) represents a rotation of the covariance matrix $\mathbf{V}^{\text{cond}}(0)$ due to the free quantum oscillation of the oscillator; the second term is contributed by thermal decoherence, which causes an increase in the uncertainty.

In the free-mass regime and for the case of $\omega_m \tau_E \ll 1$, elements of the covariance matrix can be expanded as series of Φ. Up to the leading order in Φ, we obtain

$$V_{xx}(\tau_E) = V_{xx}^{\text{cond}} + \frac{4\delta x_q^2}{\hbar} V_{xp}^{\text{cond}} \Omega_q \tau_E + \frac{\delta x_q^2}{\delta p_q^2} V_{pp}^{\text{cond}} (\Omega_q \tau_E)^2$$
$$+ 2\delta x_q^2 \zeta_F^2 \frac{(\Omega_q \tau_E)^3}{3}, \quad (50)$$

$$V_{xp}(\tau_E) = V_{xp}^{\text{cond}} + \frac{\hbar}{2\delta p_q^2} V_{pp}^{\text{cond}} \Omega_q \tau_E + \frac{\hbar}{2} \zeta_F^2 (\Omega_q \tau_E)^2, \quad (51)$$

$$V_{pp}(\tau_E) = V_{pp}^{\text{cond}} + 2\delta p_q^2 \zeta_F^2 \Omega_q \tau_E \quad (52)$$

with $V_{xx,xp,pp}^{\text{cond}}$ denoting the elements of $\mathbf{V}^{\text{cond}}(0)$. Up to the leading order in $\Omega_q \tau_E$, the uncertainty product of the resulting quantum state is

$$U(\tau_E) = \frac{2}{\hbar}\sqrt{\det \mathbf{V}(\tau_E)} \approx U(0) + \frac{V_{xx}^{\text{cond}}}{\delta x_q^2}(\tau_E/\tau_F)^2 \quad (53)$$

---

[2]Were the light turned on, the back action can still be evaded as long as one measures the amplitude quadrature $\hat{a}_1$ during this period and takes them into account during data processing. Since no information of the oscillator position (contained in the phase quadrature of outgoing light) is collected, this is equivalent to the case with the light turned off.

with τ_F defined in Eq. (22). The second term is contributed by the thermal decoherence and can be viewed as $U^{\text{th}}(\tau_E)$. Those formulas recover the results in Eqs. (29)–(32) but with precise numerical factors. As we can conclude from Eq. (53), in order for a sub-Heisenberg tomography to be possible, the later verification stage should finish within a time scale of τ_F, after which the contribution from the thermal noise gives $U^{\text{th}}(\tau_F) \sim 1$.

V. STATE VERIFICATION IN THE PRESENCE OF MARKOVIAN NOISES

In this section, we will treat the followup state verification stage with Markovian noises in detail. This can justify the order-of-magnitude estimate we have done in the Sec. III D. In addition, we will show explicitly how to construct the optimal verification scheme that gives a sub-Heisenberg accuracy.

A. A time-dependent homodyne detection and back-action-evading

In this section, we will analyze the time-dependent homodyne detection which enables us to probe mechanical quadratures. We will further show how the BAE scheme can be constructed. The BAE scheme is optimal only when there is no readout loss ($\eta = 0$). We will consider more general situations and derive the corresponding optimal verification scheme in the next section.

The equations of motion for the oscillator during the verification stage ($t > \tau_E$) are given by Eqs. (12) and (13). The corresponding solution to oscillator position is different from Eq. (46) due to the presence of the back-action noise, which starts to act on the oscillator at $t = \tau_E$. Specifically, it reads

$$\hat{x}(t) = \hat{x}_q(t) + \int_{\tau_E}^{\infty} dt' G_x(t - t')[\alpha \hat{a}_1(t') + \hat{\xi}_F(t')]. \quad (54)$$

Here the free quantum oscillation $x_q(t)$ is the signal that we seek to probe during the verification stage. For optical quadratures, the equations of motion are given by Eqs. (15) and (16). From those equations, we notice that, among the outgoing fields, $\hat{b}_1$ is pure noise, while $\hat{b}_2$ contains both signal $\hat{x}_q(t)$ and noise. In order to highlight this, we rewrite $\hat{b}_{1,2}$ as

$$\hat{b}_1(t) = \sqrt{1-\eta}\,\hat{n}_1(t) + \sqrt{\eta}\,\hat{a}_1(t) \equiv \delta\hat{b}_1(t), \quad (55)$$

$$\hat{b}_2(t) = \delta\hat{b}_2(t) + \sqrt{1-\eta}(\alpha/\hbar)\hat{x}_q(t) \quad (56)$$

with [cf. Eq. (54)]

$$\delta\hat{b}_2(t) \equiv \sqrt{\eta}\,\hat{n}_2(t) + \sqrt{1-\eta}\left\{\hat{a}_2(t) + \frac{\alpha}{\hbar}\hat{\xi}_x(t)\right.$$
$$\left. + \frac{\alpha}{\hbar}\int_{\tau_E}^{\infty} dt' G_x(t-t')[\alpha\hat{a}_1(t') + \hat{\xi}_F(t')]\right\}. \quad (57)$$

In this way, we can directly see that $\hat{a}_1$, which causes the back action, is contained in both the amplitude quadrature $\hat{b}_1$ and the phase quadrature $\hat{b}_2$. Therefore, by measuring an appropriate combination of the two output quadratures, we will be able to remove effects of the back-action noise that is imposed onto the oscillator during the verification process at $t > \tau_E$.
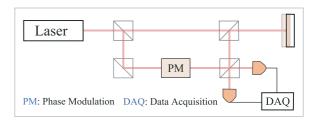

FIG. 7. (Color online) A schematic plot of time-dependent homodyne detection. The phase modulation of the local oscillator light varies in time.

Searching for such an optimal combination is the main issue to be addressed in this section.

As mentioned in the introduction, to probe mechanical quadratures and their distributions, a time-dependent homodyne detection needs to be applied [cf. Eq. (6)]. Specifically, the outgoing optical field

$$\hat{B}_{\text{out}}(t) = \hat{b}_1(t)\cos\omega_0 t + \hat{b}_2(t)\sin\omega_0 t \quad (58)$$

at $t > \tau_E$ is mixed with a strong local-oscillator light $L(t)$ whose phase angle ϕ_{os} is time-dependent as shown schematically in Fig. 7, namely,

$$L(t) = L_0 \cos[\omega_0 t - \phi_{os}(t)] \quad (59)$$

with L_0 a time-independent constant. Through a low-pass filtering (with a bandwidth much smaller than ω_0) of the beating signal, the resulting photocurrent is

$$\hat{i}(t) \propto 2\overline{\hat{B}_{\text{out}}(t)L(t)}$$
$$= L_0\hat{b}_1(t)\cos\phi_{os}(t) + L_0\hat{b}_2(t)\sin\phi_{os}(t), \quad (60)$$

where the overline means averaging over many optical-oscillation periods. Note that Heisenberg operators for the photocurrent at different time commute with each other; that is,

$$[\hat{i}(t), \hat{i}(t')] = 0, \quad (61)$$

and they are therefore *simultaneously measurable*, as obviously expected. Based on the measurement results of $\hat{i}(t)$ from τ_E to T_{int}, we can construct the following weighted quantity $\hat{Y}$ with a weight function $W(t)$:

$$\hat{Y} = \int_0^{T_{\text{int}}} \Theta(t - \tau_E)W(t)\hat{i}(t)dt \equiv (g_1|\hat{b}_1) + (g_2|\hat{b}_2). \quad (62)$$

Here the Heaviside function $\Theta(t - \tau_E)$ manifests the fact that the verification stage starts at $t = \tau_E$ and we have introduced the scalar product of two vectors $|A)$ and $|B)$ in the $\mathcal{L}^2[0, T_{\text{int}}]$ space as the following:

$$(A|B) \equiv \int_0^{T_{\text{int}}} A(t)B(t)dt. \quad (63)$$

Besides, we have defined filtering functions g_1 and g_2 as

$$g_1(t) \equiv \Theta(t - \tau_E)W(t)\cos\phi_{os}(t), \quad (64)$$

$$g_2(t) \equiv \Theta(t - \tau_E)W(t)\sin\phi_{os}(t). \quad (65)$$

Since all the data can in principle be digitalized and stored in hardware, the weight function $W(t)$ can be realized digitally during data processing. In addition, an overall rescaling of $g_{1,2}(t) \to C_0 g_{1,2}(t)$ with C_0 a time-independent constant does

not affect the verification performance, and there are multiple ways of achieving a particular set of $g_{1,2}(t)$, by adjusting the phase $\phi_{os}(t)$ of the local oscillator and the weight function $W(t)$.

In light of Eqs. (55)–(57), we decompose the weighted quantity $\hat{Y}$ [cf. Eq. (62)] as a signal $\hat{Y}_s$ and a noise part $\delta\hat{Y}$, namely,

$$\hat{Y} = \hat{Y}_s + \delta\hat{Y}. \qquad (66)$$

They are given by

$$\begin{aligned} \hat{Y}_s &= \sqrt{1-\eta}(\alpha/\hbar)(g_2|\hat{x}_q), \\ \delta\hat{Y} &= (g_1|\delta\hat{b}_1) + (g_2|\delta\hat{b}_2). \end{aligned} \qquad (67)$$

Since an overall normalization of $g_{1,2}$ will not affect the signal-to-noise ratio as mentioned, we can impose, mathematically, that

$$(g_2|f_1) = \cos\zeta, \quad (g_2|f_2) = \sin\zeta \qquad (68)$$

with

$$f_1(t) \equiv \cos\omega_m t, \quad f_2(t) \equiv (\Omega_q/\omega_m)\sin\omega_m t \qquad (69)$$

in the coordinate representation. The signal part can then be rewritten as

$$\hat{Y}_s = \sqrt{1-\eta}(\alpha/\hbar)\delta x_q \left[\hat{x}_0\cos\zeta + \hat{p}_0\sin\zeta\right], \qquad (70)$$

where we have introduced the normalized oscillator position and momentum as $\hat{x}_0 \equiv \hat{x}(\tau_E)/\delta x_q$ and $\hat{p}_0 \equiv \hat{p}(\tau_E)/\delta p_q$. In such a way, a mechanical quadrature of $\hat{X}_\zeta$ will be probed [cf. Eq. (4)]. For the noise part, more explicitly, we have [cf. Eqs. (55)–(57)]

$$\begin{aligned} \delta\hat{Y} &= (g_1|\sqrt{\eta}\hat{n}_1 + \sqrt{1-\eta}\hat{a}_1) + (g_2|\sqrt{\eta}\hat{n}_2 + \sqrt{1-\eta}\hat{a}_2) \\ &\quad + \sqrt{1-\eta}(\alpha^2/h)(g_2|\mathbf{G}_x|\hat{a}_1) \\ &\quad + \sqrt{1-\eta}(\alpha/\hbar)[(g_2|\mathbf{G}_x|\hat{\xi}_F) + (g_2|\hat{\xi}_x)], \end{aligned} \qquad (71)$$

where the integration with $G_x(t - t')$ has been augmented into applying a linear operator $\mathbf{G}_x$ in $\mathcal{L}^2[0, T_{\text{int}}]$ space. In this equation, terms on the first line comprise the shot noise, and the term on the second line is the back-action noise, while terms on the third line are the classical-force and sensing noises.

The optimal $g_1(t)$ and $g_2(t)$ that give a sub-Heisenberg accuracy for each quadrature will be rigorously derived for general situations in the next section. If $\hat{a}_1$ and $\hat{a}_2$ are uncorrelated and there is no readout loss with $\eta = 0$, an optimal choice for g_1 would be obvious to cancel the entire contribution from the back-action noise term (proportional to $\hat{a}_1$). This is equivalent to imposing, mathematically, that

$$(g_1|\hat{a}_1) + (\alpha^2/h)(g_2|\mathbf{G}_x|\hat{a}_1) = 0 \qquad (72)$$

or

$$|g_1) + (\alpha^2/h)\mathbf{G}_x^{\text{adj}}|g_2) = 0, \qquad (73)$$

where $\mathbf{G}_x^{\text{adj}}$ is the adjoint of $\mathbf{G}_x$. Physically, this corresponds to bringing in a piece of shot noise $(g_1|\hat{a}_1)$ to cancel the back-action noise $(\alpha^2/h)(g_2|\mathbf{G}_x|\hat{a}_1)$, therefore achieving a only shot-noise-limited measurement. In the coordinate representation, Eq. (73) can be written out more explicitly

as

$$g_1(t) + (\alpha^2/\hbar)\int_t^{T_{\text{int}}} dt' G_x(t' - t)g_2(t') = 0, \qquad (74)$$

which agrees exactly with the variational-type BAE measurement scheme first investigated by Vyatchanin and co-workers [50]. It is suitable for detecting signals with *known arrival time*. For stationary signals, one would prefer the frequency-domain variational techniques proposed by Kimble *et al.* [52], which evades the back-action noise for all possible signals as long as they are Gaussian and stationary.

As realized by Kimble *et al.* [52] in their frequency-domain treatment, when the readout loss is significant (large η) and when the back-action noise is strong (large α), the variational approach becomes less effective, because in such a case, the magnitude of g_1 required to bring enough $\hat{a}_1$ to cancel the back-action noise would also introduce significant noise $\hat{n}_1$ [cf. Eq. (71)]. This reasoning apparently leads to a trade-off between the need to evade back action and the need to minimize loss-induced shot noise; such an optimization will be made in the next section.

B. Optimal verification scheme and covariance matrix for the added noise: Formal derivation

Imposing the BAE condition [cf. Eq. (74)] does not specify the shape of g_2, nor does Eq. (68), and we have further freedom in choosing g_2 that minimizes the noise in measuring a particular quadrature of $\hat{X}_\zeta$. In addition, in the presence of readout loss with $\eta \neq 0$, totally evading back action is not the obvious optimum as mentioned. Therefore we need to optimize g_1 and g_2 simultaneously. In this section, we first carry out this procedure formally; we then apply it to the Markovian-noise budget in the next section.

The total $\hat{x}_q$-referred noise in the weighted estimator $\hat{Y}$ can be written as [cf. Eqs. (70) and (71)]

$$\begin{aligned} \sigma^2[g_{1,2}] &= \frac{\hbar^2}{(1-\eta)\alpha^2\delta x_q^2}\langle\delta\hat{Y}\delta\hat{Y}\rangle_{\text{sym}} \\ &= \frac{2}{(1-\eta)\Omega_q}\sum_{i,j=1}^2 (g_i|\mathbf{C}_{ij}|g_j), \end{aligned} \qquad (75)$$

where correlation functions $\mathbf{C}_{ij}$ among the noises are the following:

$$\mathbf{C}_{ij}(t, t') \equiv \langle\delta\hat{b}_i(t)\delta\hat{b}_j(t')\rangle_{\text{sym}} \quad (i, j = 1, 2). \qquad (76)$$

The optimal $g_{1,2}(t)$ that minimize σ^2 can be obtained through the standard constraint variational method. For this, we define an effective functional as

$$\begin{aligned} \mathcal{J}_{\text{eff}} &= (1-\eta)(\Omega_q/4)\sigma^2[g_{1,2}] - \mu_1(f_1|g_2) - \mu_2(f_2|g_2) \\ &= \frac{1}{2}\sum_{i,j}(g_i|\mathbf{C}_{ij}|g_j) - (\mu_1 f_1 + \mu_2 f_2|g_2), \end{aligned} \qquad (77)$$

where μ_1 and μ_2 are Lagrange multipliers due to the normalization constraints in Eq. (68). Requiring the functional

derivative of $\mathcal{J}_{\text{eff}}$ with respect to g_1 and g_2 equal to zero, we obtain

$$\mathbf{C}_{11}|g_1) + \mathbf{C}_{12}|g_2) = 0, \qquad (78)$$

$$\mathbf{C}_{21}|g_1) + \mathbf{C}_{22}|g_2) = \mu_1 f_1 + \mu_2 f_2). \qquad (79)$$

Here $\mathbf{C}_{ij}$ should be viewed as operators in $\mathcal{L}^2[0, T_{\text{int}}]$ space. This leads to formal solutions to $g_{1,2}$, namely,

$$|g_1) = -\mathbf{C}_{11}^{-1}\mathbf{C}_{12}|g_2), \qquad (80)$$

$$|g_2) = \mathbf{M}|\mu_1 f_1 + \mu_2 f_2), \qquad (81)$$

where we have defined

$$\mathbf{M} \equiv \left[\mathbf{C}_{22} - \mathbf{C}_{21}\mathbf{C}_{11}^{-1}\mathbf{C}_{12}\right]^{-1}. \qquad (82)$$

By reimposing Eqs. (68), those unknown Lagrange multipliers $\mu_{1,2}$ can be solved, which are related to ζ by

$$\begin{bmatrix} (f_1|\mathbf{M}|f_1) & (f_1|\mathbf{M}|f_2) \\ (f_2|\mathbf{M}|f_1) & (f_2|\mathbf{M}|f_2) \end{bmatrix} \begin{bmatrix} \mu_1 \\ \mu_2 \end{bmatrix} = \begin{bmatrix} \cos\zeta \\ \sin\zeta \end{bmatrix}. \qquad (83)$$

Correspondingly, the minimum $\sigma_{\min}^2$ has the following quadratic form:

$$\sigma_{\min}^2 = [\cos\zeta \ \sin\zeta]\mathbf{V}_{\text{norm}}^{\text{add}} \begin{bmatrix} \cos\zeta \\ \sin\zeta \end{bmatrix}. \qquad (84)$$

Here normalized $\mathbf{V}_{\text{norm}}^{\text{add}}$ is a 2×2 covariance matrix, and it is given by

$$\mathbf{V}_{\text{norm}}^{\text{add}} = \frac{2}{(1-\eta)\Omega_q} \begin{bmatrix} (f_1|\mathbf{M}|f_1) & (f_1|\mathbf{M}|f_2) \\ (f_2|\mathbf{M}|f_1) & (f_2|\mathbf{M}|f_2) \end{bmatrix}^{-1}. \qquad (85)$$

It relates to the initial definition of the covariance matrix for the added verification noise [cf. Eq. (8)] simply by

$$\mathbf{V}^{\text{add}} = \text{Diag}[\delta x_q, \delta p_q]\mathbf{V}_{\text{norm}}^{\text{add}}\text{Diag}[\delta x_q, \delta p_q]. \qquad (86)$$

Due to the linearity in Eqs. (79) and (83), the optimal $g_{1,2}$ for a given quadrature ζ can also be rewritten formally as

$$g_{1,2}^{\zeta} = g_{1,2}^X \cos\zeta + g_{1,2}^P \sin\zeta, \qquad (87)$$

with $g_{1,2}^X \equiv g_{1,2}^\zeta(0)$ and $g_{1,2}^P \equiv g_{1,2}^\zeta(\pi/2)$. Such a ζ dependence of $g_{1,2}$ manifests the fact that a sub-Heisenberg tomography requires different filtering functions, or equivalently different measurement setups, for different quadratures.

C. Optimal verification scheme with Markovian noise

Given Makovian noises, the corresponding correlation functions for the output noise $\delta\hat{b}_i$ can be written out explicitly as [cf. Eqs. (14), (19), (20), and (76)]

$$C_{11}(t, t') = \frac{\eta + (1-\eta)e^{2q}}{2}\delta(t-t'), \qquad (88)$$

$$C_{12}(t, t') = C_{21}(t', t) = (1-\eta)\frac{e^{2q}\alpha^2}{2\hbar}G_x(t'-t), \quad (89)$$

$$C_{22}(t, t') = \frac{\Lambda^2}{4}\delta(t-t') + (1-\eta)\frac{\alpha^4}{\hbar^2}\left(\frac{e^{2q}}{2} + \zeta_F^2\right)$$

$$\times \int_0^\infty dt_1 G_x(t-t_1)G_x(t'-t_1), \qquad (90)$$

with $\Lambda \equiv \sqrt{2[\eta + (1-\eta)(e^{-2q} + 2\zeta_x^2)]}$. Plugging these C_{ij} into Eq. (80) and (81), we can obtain the equations for the optimal filtering functions g_1 and g_2. Specifically, for g_1, we have [cf. Eq. (80)]

$$g_1(t) + \frac{(1-\eta)e^{2q}}{\eta + (1-\eta)e^{2q}}\frac{\alpha^2}{\hbar}\int_t^{T_{\text{int}}} dt' G_x(t'-t)g_2(t') = 0. \qquad (91)$$

For g_2, by writing out $\mathbf{M}$ explicitly, it gives [cf. Eq. (81)]

$$\frac{\Lambda^2}{4}g_2(t) + \zeta_F'^2\frac{\alpha^4}{\hbar^2}\iint_0^{T_{\text{int}}} dt'dt_1 G_x(t-t_1)G_x(t'-t_1)g_2(t')$$

$$= \mu_1 f_1(t) + \mu_2 f_2(t), \qquad (92)$$

where we have introduced ζ_F', which is given by

$$\zeta_F' \equiv \left[\frac{\eta(1-\eta)e^{2q}}{2[\eta + (1-\eta)e^{2q}]} + (1-\eta)\zeta_F^2\right]^{1/2} \approx \left[\frac{\eta}{2} + \zeta_F^2\right]^{1/2} \qquad (93)$$

and is equal to ζ_F for no readout loss. Although here g_1 is still defined from g_2, the optimal verification strategy does not totally evade the back action, as is manifested in the term proportional to η inside the brackets of Eq. (93). In the limit of no readout loss with $\eta = 0$, it is identical to the BAE condition in Eq. (74). Typically, we have 1% readout loss ($\eta = 0.01$), squeezing $e^{2q} = 10$, and $\zeta_F = 0.2$, so this readout loss will only shift ζ_F by 6%, which is negligible. However, if the thermal noise further decreases and/or the measurement strength increases, the effect of readout loss will become significant, entering in a similar way as the frequency-domain variational measurement proposed by Kimble *et al.* [52].

These integral equations for optimal g_1 and g_2 can be solved analytically as elaborated in Appendix C, which in turn gives $\mathbf{M}$ and the corresponding $\mathbf{V}^{\text{add}}$ [cf. Eqs. (82) and (85)]. In the free-mass regime with $\Omega_q \gg \omega_m$, closed forms for optimal g_1 and g_2 can be obtained, which, in terms of $g_{1,2}^{X,P}$ [cf. Eq. (87)], are given by

$$g_1^X = g_1|_{\zeta=0} = (\Omega_q/\chi)e^{-\Omega_q\chi t}\sin\Omega_q\chi t, \qquad (94)$$

$$g_1^P = g_1|_{\zeta=\frac{\pi}{2}} = -\sqrt{2}\Omega_q e^{-\Omega_q\chi t}\sin\left(\Omega_q\chi t + \frac{\pi}{4}\right), \quad (95)$$

and

$$g_2^X = g_2|_{\zeta=0} = 2\Omega_q\chi e^{-\Omega_q\chi t}\cos\Omega_q\chi t, \qquad (96)$$

$$g_2^P = g_2|_{\zeta=\frac{\pi}{2}} = 2\sqrt{2}\Omega_q\chi^2 e^{-\Omega_q\chi t}\sin\left(\Omega_q\chi t - \frac{\pi}{4}\right), \quad (97)$$

with $\chi \equiv [\zeta_F'^2/\Lambda]^{1/2}$. The corresponding verification time scale is set by $\tau_V = (\chi\Omega_q)^{-1}$ and $\tau_q < \tau_V < \tau_F$. To illustrate the behavior of the optimal filtering functions, we show $g_{1,2}^{X,P}$ in Fig. 8. As we can see, the verification process finishes after several τ_q (i.e., in a time scale of τ_V).

The corresponding covariance matrix $\mathbf{V}^{\text{add}}$ for the added verification noise is given by

$$\mathbf{V}^{\text{add}} = \frac{1}{1-\eta} \begin{bmatrix} \Lambda^{\frac{3}{2}}\zeta_F'^{\frac{1}{2}}\delta x_q^2 & -\Lambda\zeta_F'\hbar/2 \\ -\Lambda\zeta_F'\hbar/2 & 2\Lambda^{\frac{1}{2}}\zeta_F'^{\frac{3}{2}}\delta p_q^2 \end{bmatrix}. \qquad (98)$$

A more summarizing measure of the verification accuracy is the uncertainty product of the added noise ellipse with respect to
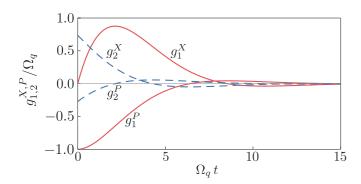
FIG. 8. (Color online) Optimal filtering functions g_1 (solid curve) and g_2 (dashed curve) in the presence of Markovian noises. We have assumed $\Omega_q/2\pi = 100$ Hz, $\zeta_x = \zeta_F = 0.2$, $\eta = 0.01$, and vacuum input ($q = 0$). For clarity, the origin of the time axis has been shifted from τ_E to 0.

to the Heisenberg limit, namely,

$$U^{\mathrm{add}} = \frac{2}{\hbar}\sqrt{\det \mathbf{V}^{\mathrm{add}}} = \frac{\Lambda \zeta_F'}{1 - \eta}. \tag{99}$$

In the ideal case with $\eta = 0$, this simply recovers the order-of-magnitude estimate given in the Sec. III D. In Fig. 9, we show the uncertainty ellipse for the added noise in the case of $\zeta_x = \zeta_F = 0.2$, readout loss $\eta = 1\%$, and with (Green dotted curve) or without (red long-dashed curve) 10-dB input squeezing. In comparison, we also plot the Heisenberg limit (unit circle) and the conditional state obtained through an ideally noiseless state preparation (blue solid ellipse). As the figure shows, the least challenging scenario already begins to characterize the conditional quantum state down to the Heisenberg uncertainty. In these two cases, we have $\Lambda = 1.48$ and 0.62, respectively, leading to

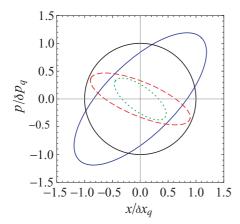$$U^{\mathrm{add}} = 0.30 \text{ (vacuum)}, \quad 0.12 \text{ (10dB squeezing)}. \tag{100}$$

FIG. 9. (Color online) The uncertainty ellipse for the added verification noise in the presence of Markovian noises. We assume $\zeta_x = \zeta_F = 0.2$, vacuum input (dashed curve), $\zeta_x = \zeta_F = 0.2$, and 10dB squeezing (dotted curve). For contrast, we also show the Heisenberg limit as a unit circle and the ideal conditional quantum state as a solid ellipse.
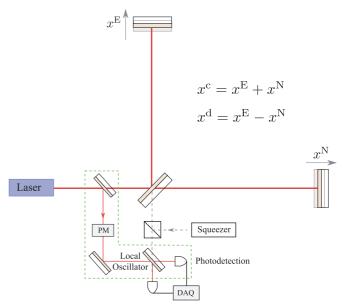

FIG. 10. (Color online) A schematic plot of advanced interferometric GW detectors for macroscopic entanglement between test masses as a test for gravity decoherence. For simplicity, we have not shown the setup at the bright port, which is identical to the dark port.

VI. VERIFICATION OF MACROSCOPIC QUANTUM ENTANGLEMENT

In this section, we will apply our protocol to verify macroscopic entanglement between test masses in future GW detectors, which was proposed in Refs. [34,35]. In the experiment, as shown schematically in Fig. 10, measurements at the bright and dark ports of the interferometer continuously collapse the quantum state of the corresponding common and differential modes of the test-mass motion. This creates two highly squeezed Gaussian states in both modes. Since the common and differential modes are linear combinations of the center-of-mass motion of test masses in the two arms, namely $\hat{x}^c = \hat{x}^E + \hat{x}^N$ and $\hat{x}^d = \hat{x}^E - \hat{x}^N$, this will naturally generate quantum entanglement between the two test masses, which is similar to creating entanglement by mixing two optical squeezed states at the beam splitter [55,56].

A. Entanglement survival time

To quantify the entanglement strength, we follow Refs. [34, 35] by evaluating the entanglement monotone—logarithmic negativity defined in Refs. [57,58]. It can be derived from the covariance matrix for the Gaussian-continuous-variable system considered here. The bipartite covariances among $(\hat{x}^E, \hat{p}^E, \hat{x}^N, \hat{p}^N)$ form the following covariance matrix:

$$\mathbf{V} = \begin{bmatrix} \mathbf{V}_{\mathrm{EE}} & \mathbf{V}_{\mathrm{EN}} \\ \mathbf{V}_{\mathrm{NE}} & \mathbf{V}_{\mathrm{NN}} \end{bmatrix}, \tag{101}$$

where

$$\mathbf{V}_{\mathrm{EE}} = \mathbf{V}_{\mathrm{NN}} = \begin{bmatrix} \left(V_{xx}^c + V_{xx}^d\right)/4 & \left(V_{xp}^c + V_{xp}^d\right)/2 \\ \left(V_{xp}^c + V_{xp}^d\right)/2 & \left(V_{pp}^c + V_{pp}^d\right) \end{bmatrix}, \tag{102}$$
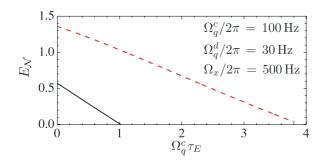
FIG. 11. (Color online) Logarithmic negative $E_\mathcal{N}$ as a function of the evolution duration τ_E, which indicates how long the entanglement survives. The solid curve corresponds to the case where $\Omega_F/2\pi = 20$Hz and the dashed curve is for $\Omega_F/2\pi = 10$Hz. To maximize the entanglement, the common mode is 10 dB phase squeezed at $t > \tau_E$ and $t < 0$ while the differential mode is 10 dB amplitude squeezed at $t < 0$ and switching to 10 dB phase squeezed at $t > \tau_E$.

$$\mathbf{V}_{\mathrm{NE}} = \mathbf{V}_{\mathrm{EN}} = \begin{bmatrix} (V_{xx}^c - V_{xx}^d)/4 & (V_{xp}^c - V_{xp}^d)/2 \\ (V_{xp}^c - V_{xp}^d)/2 & (V_{pp}^c - V_{pp}^d) \end{bmatrix}. \quad (103)$$

The logarithmic negativity $E_\mathcal{N}$ can then be written as

$$E_\mathcal{N} = \max[0, -\log_2 2\sigma_-/\hbar], \quad (104)$$

where $\sigma_- \equiv \sqrt{(\Sigma - \sqrt{\Sigma^2 - 4\det\mathbf{V}})/2}$ and $\Sigma \equiv \det\mathbf{V}_{\mathrm{NN}} + \det\mathbf{V}_{\mathrm{EE}} - 2\det\mathbf{V}_{\mathrm{NE}}$. In contrast to Refs. [34,35], now the covariance matrix $\mathbf{V}$ corresponds to the total covariance matrix $\mathbf{V}^{\mathrm{tot}}$ after the entire preparation-evolution-verification process. For Gaussian quantum states, we have [cf. Eqs. (10), (48), and (98)]

$$\mathbf{V}^{\mathrm{tot}} = \mathbf{V}(\tau_E) + \mathbf{V}^{\mathrm{add}}. \quad (105)$$

B. Entanglement survival as a test of gravity decoherece

When τ_E increases, the thermal decoherence will increase the uncertainty [cf. Eqs. (48) and (105)] and eventually the entanglement vanishes, which indicates how long the quantum entanglement can survive. Survival of such quantum entanglement can help us to understand whether there is any additional decoherence effect, such as the *gravity decoherence* suggested by Diósi and Penrose [48,49]. According to their models, quantum superpositions vanish within a time scale of $\hbar/E_G$. Here E_G can be (a) self-energy of the mass-distribution difference, namely,

$$E_G^{(a)} = \int d\mathbf{x}d\mathbf{y}\, G[\rho(\mathbf{x}) - \rho'(\mathbf{x})][\rho(\mathbf{y}) - \rho'(\mathbf{y})]/r \quad (106)$$

with ρ denoting the mass density distribution and $r \equiv |\mathbf{x} - \mathbf{y}|$, or, alternatively, (b) a spread of mutual gravitational energy among components of the quantum superposition, namely,

$$E_G^{(b)} = \int d\mathbf{x}d\mathbf{y}\, G\rho(\mathbf{x})\rho'(\mathbf{y})\delta r/r^{3/2} \quad (107)$$

with δr denoting the uncertainty in location. For the prepared test-mass quantum states with width of δx_q, we have

$$\tau_G^{(a)} \approx \Omega_q/(G\rho), \quad \tau_G^{(b)} \approx \hbar^{1/2}L^2\Omega_q^{1/2}/(Gm^{3/2}), \quad (108)$$

where L is the distance between two test masses. Plugging in the typical values of LIGO mirrors with $\rho = 2.2$ g/cm^3,

separation between two input test masses of $L \approx 10$ m, and $m = 10$ kg, we have

$$\tau_G^a = 4.3 \times 10^9 \text{ s}, \quad \tau_G^b = 1.2 \times 10^{-5} \text{ s}. \quad (109)$$

It is therefore quite implausible to test model (a), whereas for model (b), $\Omega_q\tau_G^{(b)}$ is less than 0.01 with $\Omega_q/2\pi = 100$ Hz. In Fig. 11, we show the entanglement survival as a function of evolution duration. As we can see, the model (b) of gravity decoherence can easily be tested, for the entanglement can survive for several times the measurement time scale τ_q, which is much longer than the predicted $\tau_G^{(b)}$.

VII. CONCLUSIONS

We have investigated in great detail of a follow-up verification stage after the state preparation and evolution. We have showed the necessity of a sub-Heisenberg verification accuracy in probing the prepared conditional quantum state and how to achieve it with an optimal time-domain homodyne detection. Including this essential building block—a sub-Heisenberg verification, we are able to outline a complete procedure of a three-staged experiment for testing macroscopic quantum mechanics. In particular, we have been focusing on the relevant free-mass regime and have applied the techniques to discuss MQM experiments with future GW detectors. However, the system dynamics that have been considered describe general cases with a high-Q mechanical oscillator coupled to coherent optical fields. In this respect, we note that our results for Markovian systems only depend on the ratio between various noises and the SQL and therefore carry over directly to systems with other scales. In addition, the Markovian assumption applies more accurately to smaller scale systems, which operate in higher frequencies.

APPENDIX A: NECESSITY OF SUB-HEISENBERG ACCURACY FOR REVEALING NONCLASSICALITY

As we have mentioned in the introduction, sub-Heisenberg accuracy is a necessary condition to probe the nonclassicality if the Wigner function of the prepared quantum state has some negative regions, which do not have any classical counterpart.

To prove the necessity, we use the relation between the Q function and the Wigner function as pointed out by Khalili [59].

Given density matrix $\hat{\rho}$, the Q function in the coherent state basis $|\alpha\rangle$ is equal to [31,60,61]

$$Q = \frac{1}{\pi}\langle\alpha|\hat{\rho}|\alpha\rangle, \tag{A1}$$

which is always positive defined. It is the Fourier transform of the following characteristic function:

$$J(\beta, \beta^*) = \text{Tr}[e^{i\beta^*\hat{a}}e^{i\beta\hat{a}^\dagger}\hat{\rho}]. \tag{A2}$$

Here $\hat{a}$ is the annihilation operator and is related to the normalized oscillator position $\hat{x}/\delta x_q$ and momentum $\hat{p}/\delta p_q$ [cf. Eq. (26)] by the standard relation

$$\hat{a} = [(\hat{x}/\delta x_q) + i(\hat{p}/\delta p_q)]/2. \tag{A3}$$

If we introduce the real and imaginary parts of β, namely, $\beta = \beta_{\rm r} + i\beta_{\rm i}$, characteristic function J can be rewritten as

$$J(\beta_{\rm r}, \beta_{\rm i}) = e^{-(\beta_{\rm r}^2+\beta_{\rm i}^2)/2}\text{Tr}[e^{i\beta_{\rm r}(\hat{x}/\delta x_q)+i\beta_{\rm i}(\hat{p}/\delta p_q)}\hat{\rho}], \tag{A4}$$

where we have used the fact that $e^{\hat{A}}e^{\hat{B}} = e^{\hat{A}+\hat{B}}e^{[\hat{A},\hat{B}]/2}$, as $[\hat{A}, \hat{B}]$ commutes with $\hat{A}$ and $\hat{B}$. Inside the brackets of Eq. (A4), it is the characteristic function for the Wigner function $W(x, p)$, and thus

$$J(\beta_{\rm r}, \beta_{\rm i}) = \frac{1}{(2\pi)^2}\int dx' dp' e^{-(\beta_{\rm r}^2+\beta_{\rm i}^2)/2}$$
$$\times e^{-i\beta_{\rm r}(x'/\delta x_q)-i\beta_{\rm i}(p'/\delta p_q)}W(x', p'). \tag{A5}$$

By integrating over $\beta_{\rm i}$ and $\beta_{\rm i}$, the resulting Q function is given by

$$Q(x, p) = \frac{1}{2\pi}\int dx' dp' e^{-\frac{1}{2}\left[\frac{(x-x')^2}{\delta x_q^2}+\frac{(p-p')^2}{\delta p_q^2}\right]}W(x', p'). \tag{A6}$$

This will be the same as Eq. (7), if we identify $W_{\rm recon}(x, p)$ with $Q(x, p)$ and

$$\mathbf{V}^{\rm add} = \begin{bmatrix} \delta x_q^2 & 0 \\ 0 & \delta p_q^2 \end{bmatrix}, \tag{A7}$$

which is a Heisenberg-limited error. Since squeezing and a rotation of $\hat{x}$ and $\hat{p}$ axes will not change the positivity of the Q function, Eq. (A6) basically dictates that the reconstructed Wigner function will always be positive if a Heisenberg-limited error is introduced during the verification stage. Therefore, only if sub-Heisenberg accuracy is achieved will we be able to reveal the nonclassicality of the prepared quantum state.

APPENDIX B: WIENER-HOPF METHOD FOR SOLVING INTEGRAL EQUATIONS

In this Appendix, we will introduce the mathematical method invented by N. Wiener and E. Hopf for solving a special type of integral equation. For more details, one can refer to a comprehensive presentation of this method and its applications by Noble [62]. Here we will focus on integral equations that can be brought into the following form as encountered in obtaining the optimal verification scheme:

$$\int_0^{+\infty} dt' C(t, t')g(t') = h(t), \quad t > 0, \tag{B1}$$

with

$$C(t, t') = A(t - t') + \sum_\alpha \int_0^{\min[t,t']} dt'' B_\alpha^*(t-t'')B_\alpha(t'-t''), \tag{B2}$$

where $\alpha = 1, 2, \ldots$ and $B_\alpha(t) = 0$ if $t < 0$.

Assuming the solution to $g(t)$ be a square-integrable function in $\mathcal{L}^2(-\infty, \infty)$, one can split it into *causal* and *anticausal* parts as

$$g(t) = g_+(t) + g_-(t), \tag{B3}$$

where $g_-(t)$ is the *causal* part:

$$g_-(t) = \begin{cases} 0, & t > 0, \\ g(t), & t \leqslant 0, \end{cases} \tag{B4}$$

and $g_+(t)$ is the *anticausal* part of $g(t)$:

$$g_+(t) = \begin{cases} g(t), & t > 0, \\ 0, & t \leqslant 0. \end{cases} \tag{B5}$$

This definition enables us to expand the limits of integration in (B1) and (B2) to $-\infty < (t, t', t'') < \infty$:

$$\int_{-\infty}^{+\infty} dt' C(t, t')g_+(t') = h(t), \quad t > 0, \tag{B6}$$

where

$$C(t, t') = A(t - t')$$
$$+ \sum_\alpha \int_{-\infty}^{+\infty} dt''[B_{\alpha,+}^*(t - t'')B_{\alpha,+}(t' - t'')]_{(+,t'')}, \tag{B7}$$

and index $(+, t'')$ stands for taking causal part of a multidimensional function in the argument t''.

Let us first exercise the method in a simple special case when $B_\alpha(t) \equiv 0$; $\forall\alpha$, this gives a conventional Wiener-Hopf integral equation

$$\int_0^{+\infty} dt' A(t - t')g(t') = h(t), \quad t > 0, \tag{B8}$$

which can be rewritten as

$$\left[\int_{-\infty}^{+\infty} dt' A(t - t')g_+(t') - h(t)\right]_{(+,t)} = 0. \tag{B9}$$

Applying the Fourier transform in t and the convolution theorem, one gets

$$\int_{-\infty}^{+\infty} \frac{d\Omega}{2\pi}[\tilde{A}(\Omega)\tilde{g}_+(\Omega) - \tilde{h}(\Omega)]_+ e^{-i\Omega t} = 0. \tag{B10}$$

The spectrum of the causal (anticausal) function is simply

$$\tilde{g}_{+(-)}(\Omega) = \int_{-\infty}^{\infty} dt g_{+(-)}(t)e^{i\Omega t}. \tag{B11}$$

However, this evident relation is not operational for us, as it provides no intuition on how to directly get $\tilde{g}_\pm(\Omega)$ given $\tilde{g}(\Omega)$ in disposal. The surprisingly simple answer gives complex analysis. Without loss of generality, we can assume that $g(t)$ asymptotically goes to zero at infinity as $\forall t : |g(t)| < e^{-\gamma_0|t|}$, where γ_0 is some arbitrary positive number, that guarantees

regularity of $\tilde{g}(\Omega)$ at $-\infty < \Omega < \infty$. In terms of analytic continuation $\tilde{g}(s)$ of $\tilde{g}(\Omega)$ to the complex plane $s = \Omega + i\gamma$, this assumption means that all the poles of $\tilde{g}(s)$ are located outside its band of analyticity, $-\gamma_0 < \text{Im}(s) < \gamma_0$. Thus, the partition into causal and anticausal parts for $\tilde{g}(s)$ is now evident:

$$\tilde{g}(s) = \tilde{g}_+(s) + \tilde{g}_-(s), \quad (B12)$$

where $\tilde{g}_+(s)[\tilde{g}_-(s)]$ stands for the function equal to $\tilde{g}(s)$ for $\gamma > \gamma_0 (< -\gamma_0)$ and analytic in the half-plane above (below) the line $\gamma = \gamma_0(-\gamma_0)$.[3] According to the properties of analytic continuation, this decomposition is unique and completely determined by values of $\tilde{g}(\Omega)$ on the real axis. Moreover, as a Fourier transform of a valid $\mathcal{L}^2$ function, it has to approach zero when $|s| \to \infty$. For more general cases, this requirement could be relaxed to demand that ∞ should be a regular point of $\tilde{g}(s)$ so that $\lim_{|s|\to\infty} \tilde{g}(s) = \text{const}$. This allows us to include the δ function and other integrable distributions, though it makes us add the constant $g(\infty)$ to formula (B12) as an additional term. For example, for $g(t) = e^{-\alpha|t|}$, $\alpha > 0$, one has the following fourier transform:

$$\tilde{g}(s) = \frac{2\alpha}{\alpha^2 + s^2} = \frac{2\alpha}{(s + i\alpha)(s - i\alpha)}, \quad (B13)$$

which has one pole $s_+ = -i\alpha$ in the lower half complex plane (LHP) and one pole $s_- = +i\alpha$ in the upper half complex plane (UHP). To split $\tilde{f}(\Omega)$ in accordance with (B12) one can use well-known formula

$$\tilde{g}_{\pm}(s) = \sum_{\{s_{\pm,k}\}} \frac{\text{Res}[\tilde{g}(s), s_{\pm,k}]}{(s - s_{\pm,k})^{\sigma_k}}, \quad (B14)$$

where summation goes over all poles $\{s_{+,k}\}$ (with σ_k the order of pole $s_{+,k}$) of $\tilde{g}(s)$ that belong to the LHP for $\tilde{g}_+(s)$ and over all poles $\{s_{-,k}\}$ of $\tilde{g}(s)$ that belong to the UHP for $\tilde{g}_-(s)$ otherwise, and $\text{Res}[\tilde{g}(s), s]$ stands for residue of $\tilde{g}(s)$ at pole s. For our example function this formula gives

$$\tilde{g}_+(s) = \frac{i}{s + i\alpha}, \quad \tilde{g}_-(s) = -\frac{i}{s - i\alpha}. \quad (B15)$$

Using the residue theorem, one can easily show that

$$g_+(t) = e^{-\alpha t}, \quad \text{for } t > 0, \quad (B16)$$

$$g_-(t) = e^{\alpha t}, \quad \text{for } t < 0. \quad (B17)$$

Returning to Eq. (B10), we assume that function $\tilde{A}(\Omega)$ can be factorized in the following way:

$$\tilde{A}(\Omega) = \tilde{a}_-(\Omega)\tilde{a}_+(\Omega), \quad (B18)$$

where $\tilde{a}_{+(-)}(\Omega)$ is a function analytic in the UHP (LHP) with its inverse, that is, both its poles and zeroes, being located in the LHP (UHP). One gets the following equation:

$$[\tilde{a}_-(\Omega)\tilde{a}_+(\Omega)\tilde{g}_+(\Omega) - \tilde{h}(\Omega)]_+ = 0. \quad (B19)$$

To solve this equation, one realizes the following fact: For any function $\tilde{f}$, $[\tilde{f}(\Omega)]_+ = 0$ means that $\tilde{f}$ has no poles in the LHP. Multiplication of $\tilde{f}$ by any function $\tilde{g}_-$ which also has no poles

in the LHP will evidently not change the equality; namely, $[\tilde{g}_-(\Omega)\tilde{f}(\Omega)]_+ = 0$. By multiplying Eq. (B19) by $1/\tilde{a}_-(\Omega)$, the solution reads

$$\tilde{g}_+(\Omega) = \frac{1}{\tilde{a}_+(\Omega)} \left[\frac{\tilde{h}(\Omega)}{\tilde{a}_-(\Omega)} \right]_+. \quad (B20)$$

By performing the inverse Fourier transform of $\tilde{g}_+(\Omega)$, the time-domain solution $g_+(t)$ can be obtained.

Now we are ready to solve Eq. (B6) with the general kernel in Eq. (B7). Performing similar manipulations, one obtains the following equation for $\tilde{g}_+(\Omega)$ in the Fourier domain:

$$\left[\left(\tilde{A} + \sum_\alpha \tilde{B}_\alpha \tilde{B}_\alpha^* \right) \tilde{g}_+ - \sum_\alpha \tilde{B}_\alpha (\tilde{B}_\alpha^* \tilde{g}_+)_- - \tilde{h} \right]_+ = 0, \quad (B21)$$

where we have omitted arguments Ω of all functions for brevity. Since $\tilde{B}_\alpha$ is a causal function, $\tilde{B}_\alpha^*$ is anticausal, and $\tilde{g}_+$ is causal, $(\tilde{B}_\alpha^* \tilde{g})_-$ only depends on the value of $\tilde{g}$ on the poles of $\tilde{B}_\alpha^*$. Performing a similar factorization

$$\tilde{\psi}_+ \tilde{\psi}_- = \tilde{A} + \sum_\alpha \tilde{B}_\alpha \tilde{B}_\alpha^* \quad (B22)$$

with $\tilde{\psi}_+$ ($\tilde{\psi}_-$) and $1/\tilde{\psi}_+$ ($1/\tilde{\psi}_-$) analytic in the UHP (LHP), $\psi_+(-\Omega) = \psi_+^*(\Omega) = \psi_-(\Omega)$, we get the solution in the form

$$\tilde{g}_+ = \frac{1}{\tilde{\psi}_+} \left[\frac{\tilde{h}}{\tilde{\psi}_-} \right]_+ + \frac{1}{\tilde{\psi}_+} \left[\sum_\alpha \frac{\tilde{B}_\alpha (\tilde{B}_\alpha^* \tilde{g}_+)_-}{\tilde{\psi}_-} \right]_+. \quad (B23)$$

Although $\tilde{g}_+$ also enters the right-hand side of this equation, $(\tilde{B}_\alpha^* \tilde{g}_+)_-$ can be written out explicitly as

$$(\tilde{B}_\alpha^* \tilde{g}_+)_- = \sum_{\{\Omega_{-,k}\}} \frac{\tilde{g}_+(\Omega_{-,k})\text{Res}[\tilde{B}^*(\Omega), \Omega_{-,k}]}{(\Omega - \Omega_{-,k})^{\sigma_k}}. \quad (B24)$$

Here $\{\Omega_{-,k}\}$ are poles of $\tilde{B}^*(\Omega)$ that belong to UHP, and therefore $\tilde{g}_+(\Omega_{-,k})$ are just constants that can be obtained by solving a set of linear algebraic equations evaluating Eq. (B23) at those poles $\{\Omega_{-,k}\}$.

APPENDIX C: SOLVING INTEGRAL EQUATIONS IN SEC. V

Here we will use the technique introduced in the Appendix B to obtain analytical solutions to the integral equations we encountered in the Secs. V B and V C.

In the coordinate representation, the integral equations for $g_{1,2}$ are the following [cf. Eqs. (78) and (79)]:

$$\int_0^{T_{\text{int}}} dt' \begin{bmatrix} \mathbf{C}_{11}(t, t') & \mathbf{C}_{12}(t, t') \\ \mathbf{C}_{21}(t, t') & \mathbf{C}_{22}(t, t') \end{bmatrix} \begin{bmatrix} g_1(t') \\ g_2(t') \end{bmatrix} = \begin{bmatrix} 0 \\ h(t) \end{bmatrix}, \quad (C1)$$

where $\mathbf{C}_{ij}(i, j = 1, 2)$ are given by Eq. (88) and we have defined $h(t) \equiv \mu_1 f_1(t) + \mu_2 f_2(t)$. Since the optimal $g_{1,2}(t)$ will automatically cut off when $t > \tau_F$, we can extend the integration upper bound T_{int} to ∞. This brings those equations into the right shape considered in Appendix B. In the frequency domain, they can be written as

$$[\tilde{S}_{11}\tilde{g}_1]_+ + [\tilde{S}_{12}\tilde{g}_2]_+ = 0, \quad (C2)$$

$$[\tilde{S}_{21}\tilde{g}_1]_+ + [\tilde{S}_{22}\tilde{g}_2]_+ - \tilde{\Gamma} = \tilde{h}, \quad (C3)$$

$$\tilde{\Gamma} = (1 - \eta)(\Omega_q^4/2)(e^{2q} + 2\zeta_F^2)[\tilde{G}_x(\tilde{G}_x\tilde{g}_2)_-]_+. \quad (C4)$$

---

[3]Functions $\tilde{g}_+(s)$ and $\tilde{g}_-(s)$ are, in essence, Laplace transforms of $g(t)$ for positive and negative time, respectively, with only substitution of variable $s \to ip$.

Here $\tilde{S}_{ij}$ are the Fourier transformation of the correlation functions $\mathbf{C}_{ij}$. Specifically, they are

$$\tilde{S}_{11} = \frac{\eta + (1-\eta)e^{2q}}{2}, \tag{C5}$$

$$\tilde{S}_{12} = -\frac{(1-\eta)e^{2q}\Omega_q^2}{2(\Omega + \omega_m - i\gamma_m)(\Omega - \omega_m - i\gamma_m)}, \tag{C6}$$

$$\tilde{S}_{21} = \tilde{S}_{12}^*, \tag{C7}$$

$$\tilde{S}_{22} = \frac{\Lambda^2}{4} + \frac{(1-\eta)(e^{2q} + 2\zeta_F^2)\Omega_q^4}{2[(\Omega + \omega_m)^2 + \gamma_m^2][(\Omega - \omega_m)^2 + \gamma_m^2]}. \tag{C8}$$

Since $\tilde{S}_{11}$ is only a number, the solution to $\tilde{g}_1$ is simply

$$\tilde{g}_1 = -\tilde{S}_{11}^{-1}[\tilde{S}_{12}\tilde{g}_2]_+. \tag{C9}$$

In the time domain, this recovers the result in Eq. (91). Through a spectral factorization

$$\tilde{\psi}_+\tilde{\psi}_- \equiv \tilde{S}_{22} - \tilde{S}_{11}^{-1}\tilde{S}_{12}\tilde{S}_{21}, \tag{C10}$$

we obtain the solution for $\tilde{g}_2$:

$$\tilde{g}_2 = \frac{1}{\tilde{\psi}_+}\left\{\frac{1}{\tilde{\psi}_-}\left[\tilde{h} - \tilde{S}_{11}^{-1}\tilde{S}_{21}(\tilde{S}_{12}\tilde{g}_2)_- + \tilde{\Gamma}\right]\right\}_+. \tag{C11}$$

By plugging $\tilde{\Gamma}$ into this equation, $\tilde{g}_2$ becomes

$$\tilde{g}_2 = \frac{1}{\tilde{\psi}_+}\left\{\frac{1}{\tilde{\psi}_-}\left[\tilde{h} + \kappa\tilde{G}_x(\tilde{G}_x^*\tilde{g}_2)_-\right]\right\}_+ \tag{C12}$$

with $\kappa \equiv m^2\Omega_q^4\zeta_F'^2$. A simple inverse Fourier transformation gives $g_1(t)$ and $g_2(t)$. The unknown Lagrange multipliers can be solved using Eq. (83). We can then derive the covariance matrix $\mathbf{V}^{\mathrm{add}}$ for the added verification noise with Eq. (85). In the free-mass regime, a closed form for $\mathbf{V}^{\mathrm{add}}$ can be obtained as shown explicitly in Eq. (98).

[1] C. Metzger, and K. Karrai, Nature (London) **432**, 1002 (2004).

[2] S. Gigan, H. R. Böhm, M. Paternostro, F. Blaser, G. Langer, J. B. Hertzberg, K. C. Schwab, D. Bäuerle, M. Aspelmeyer, and A. Zeilinger, Nature (London) **444**, 67 (2006).

[3] O. Arcizet, P. Cohandon, T. Briant, M. Pinard, and A. Heidmann, Nature (London) **444**, 71 (2006).

[4] D. Kleckner and D. Bouwmeester, Nature (London) **444**, 75 (2006).

[5] A. Schliesser, P. DelHaye, N. Nooshi, K. J. Vahala, and T. Kippenberg, Phys. Rev. Lett. **97**, 243905 (2006).

[6] T. Corbitt, Y. Chen, E. Innerhofer, H. Muller-Ebhardt, D. Ottaway, H. Rehbein, D. Sigg, S. Whitcomb, C. Wipf, and N. Mavalvala, Phys. Rev. Lett. **98**, 150802 (2007).

[7] T. Corbitt, C. Wipf, T. Bodiya, D. Ottaway, D. Sigg, N. Smith, S. Whitcomb, and N. Mavalvala, Phys. Rev. Lett. **99**, 160801 (2007).

[8] A. Schliesser, R. Rivire, G. Anetsberger, O. Arcizet, and T. Kippenberg, Nature Phys. **4**, 415 (2008).

[9] I. Favero, C. Metzger, S. Camerer, D. König, H. Lorenz, J. Kotthaus, and K. Karrai, Appl. Phys. Lett. **90**, 104101 (2007).

[10] J. D. Teufel, J. R. Harlow, C. A. Regal, and K. W. Lehnert, Phys. Rev. Lett. **101**, 197203 (2008).

[11] J. Thompson, B. Zwickl, A. Jayich, F. Marquardt, S. Girvin, and J. Harris, Nature (London) **452**, 72 (2008).

[12] C. M. Mow-Lowry, A. J. Mullavey, S. Gossler, M. B. Gray, and D. E. McClelland, Phys. Rev. Lett. **100**, 010801 (2008).

[13] S. Gröblacher, S. Gigan, H. R. Böhm, A. Zeilinger, and M. Aspelmeyer, EPL **81**, 54003 (2008).

[14] S. W. Schediwy, C. Zhao, L. Ju, D. G. Blair, and P. Willems, Phys. Rev. A **77**, 013813 (2008).

[15] G. Jourdan, F. Comin, and J. Chevrier, Phys. Rev. Lett. **101**, 133904 (2008).

[16] S. Gröblacher, J. Hertzberg, M. Vanner, G. Cole, S. Gigan, K. Schwab, and M. Aspelmeyer, Nature Phys. **5**, 485 (2009).

[17] D. G. Blair, E. N. Ivanov, M. E. Tobar, P. J. Turner, F. van Kann, and I. S. Heng, Phys. Rev. Lett. **74**, 1908 (1995).

[18] A. Naik, O. Buu, M. LaHaye, A. D. Armour, A. Clerk, M. Blencowe, and K. Schwab, Nature (London) **443**, 193 (2006).

[19] T. Rocheleau, T. Ndukum, C. Macklin, J. Hertzberg, A. Clerk, and K. Schwab, e-print arXiv:0907.3313v1 (2009).

[20] P. F. Cohadon, A. Heidmann, and M. Pinard, Phys. Rev. Lett. **83**, 3174 (1999).

[21] M. Poggio, C. L. Degen, H. J. Mamin, and D. Rugar, Phys. Rev. Lett. **99**, 017201 (2007).

[22] B. Abbott *et al.* (LIGO Scientific Collaboration), New J. Phys. **11**, 073032 (2009).

[23] S. Vyatchanin, Dokl. Akad. Nauk SSSR **234**, 1295 (1977).

[24] S. Mancini, D. Vitali, and P. Tombesi, Phys. Rev. Lett. **80**, 688 (1998).

[25] F. Marquardt, J. P. Chen, A. A. Clerk, and S. M. Girvin, Phys. Rev. Lett. **99**, 093902 (2007).

[26] I. Wilson-Rae, N. Nooshi, W. Zwerger, and T. J. Kippenberg, Phys. Rev. Lett. **99**, 093901 (2007).

[27] C. Genes, D. Vitali, P. Tombesi, S. Gigan, and M. Aspelmeyer, Phys. Rev. A **77**, 033804 (2008).

[28] S. Danilishin, H. Müller-Ebhardt, H. Rehbein, K. Somiya, R. Schnabel, K. Danzmann, T. Corbitt, C. Wipf, N. Mavalvala, and Y. Chen, e-print arXiv:0809.2024 [quant-ph] (2008).

[29] A. Barchielli, Int. J. Theor. Phys. **32**, 2221 (1992).

[30] A. Hopkins, K. Jacobs, S. Habib, and K. Schwab, Phys. Rev. B **68**, 235328 (2003).

[31] C. W. Gardiner, and P. Zoller, *Quantum Noise* (Springer-Verlag, New York, 1996).

[32] G. J. Milburn, Quantum Semiclass. Opt. **8**, 269 (1996).

[33] A. C. Doherty, S. M. Tan, A. S. Parkins, and D. F. Walls, Phys. Rev. A **60**, 2380 (1999).

[34] H. Müller-Ebhardt, H. Rehbein, R. Schnabel, K. Danzmann, and Y. Chen, Phys. Rev. Lett. **100**, 013601 (2008).

[35] H. Müller-Ebhardt, H. Rehbein, C. Li, Y. Mino, K. Somiya, R. Schnabel, K. Danzmann, and Y. Chen, Phys. Rev. A **80**, 043802 (2009).

[36] http://www.ligo.caltech.edu/advLIGO.

[37] S. Miyoki, T. Uchiyama, K. Yamamoto, H. Hayakawa, K. Kasahara, H. Ishitsuka, M. Ohashi, K. Kuroda, and D. Tatsumi, Class. Quantum Grav. **21**, 1173 (2004).

[38] V. B. Braginsky, JETP **26**, 831 (1968).

[39] C. M. Caves, K. S. Thorne, R. W. Drever, V. D. Sandberg, and M. Zimmermann, Rev. Mod. Phys. **52**, 341 (1980).

[40] V. B. Braginsky and F. Y. Khalili, *Quantum Measurement* (Cambridge University Press, Cambridge, 1992).

[41] Recent review paper by A. I. Lvovsky and M. G. Raymer, Rev. Mod. Phys. **81**, 299 (2009).

[42] B. Yurke and D. Stoler, Phys. Rev. A **36**, 1955R (1987).

[43] S. Mancini, V. I. Man'ko, and P. Tombesi, Phys. Rev. A **55**, 3042 (1997).

[44] S. Bose, K. Jacobs, and P. I. Knight, Phys. Rev. A **56**, 4175 (1997).

[45] I. Katz, A. Retzker, R. Straub, and R. Lifshitz, Phys. Rev. Lett. **99**, 040404 (2007).

[46] K. Jacobs, Phys. Rev. Lett. **99**, 117203 (2007).

[47] F. Ya. Khalili *et al.* (in preparation).

[48] L. Diósi, Phys. Lett. **A120**, 377 (1987); Phys. Rev. A **40**, 1165; J. Phys. A **40**, 2989 (2007).

[49] R. Penrose, Gen. Rel. Grav. **28**, 581 (1996); Philos. Trans. R. Soc. London Ser. A **356**, 1927; *The Road to Reality: A Complete Guide to the Laws of the Universe* (Knopf, New York, 2005).

[50] S. P. Vyatchanin and A. B. Matsko, JETP **77**, 218 (1993); S. P. Vyatchanin and E. A. Zubova, Phys. Lett. **A201**, 269 (1995); S. P. Vyatchanin, *ibid.* **A239**, 201 (1998); S. P. Vyatchanin and A. B. Matsko, JETP **82**, 1007 (1996); **83**, 690 (1996).

[51] Y. Chen *et al.* (in preparaion).

[52] H. J. Kimble, Y. Levin, A. B. Matsko, K. S. Thorne, and S. P. Vyatchanin, Phys. Rev. D **65**, 022002 (2001); P. Purdue, *ibid.* **66**, 022001 (2002); P. Purdue and Y. Chen, *ibid.* **66**, 122004 (2002).

[53] C. M. Caves and B. L. Schumaker, Phys. Rev. A **31**, 3068 (1985).

[54] K. J. Blow, R. Loudon, S. J. D. Phoenix, and T. J. Shepherd, Phys. Rev. A **42**, 4102 (1990).

[55] A. Furusawa, J. L. Sørensen, S. L. Braunstein, C. A. Fuchs, H. J. Kimble, and E. S. Polzik, Science **282**, 706 (1998).

[56] W. P. Bowen, R. Schnabel, P. K. Lam, and T. C. Ralph, Phys. Rev. Lett. **90**, 043601 (2003).

[57] G. Vidal and R. F. Werner, Phys. Rev. A **65**, 032314 (2002).

[58] G. Adesso, A. Serafini, and F. Illuminati, Phys. Rev. A **70**, 022318 (2004).

[59] F. Ya. Khalili (private communications).

[60] M. O. Scully and M. S. Zubairy, *Quantum Optics* (Cambridge University Press, Cambridge, 1997).

[61] D. F. Walls and G. Milburn, *Quantum Optics*, 2nd ed. (Springer-Verlag, New York, 2008).

[62] B. Noble, *Methods Based on the Wiener-Hopf Technique for the Solution of Partial Differential Equations* (AMS Chelsea, Providence, 1988).